

Bayesian inference for group-level cortical surface image-on-scalar-regression with Gaussian process priors

Andrew S. Whiteman,* Timothy D. Johnson, and Jian Kang

*awhitem@umich.edu

Department of Biostatistics,
University of Michigan, Ann Arbor,
Michigan, U.S.A.

Abstract

In regression-based analyses of group-level neuroimage data researchers typically fit a series of marginal general linear models to image outcomes at each spatially-referenced pixel. Spatial regularization of effects of interest is usually induced indirectly by applying spatial smoothing to the data during preprocessing. While this procedure often works well, resulting inference can be poorly calibrated. Spatial modeling of effects of interest leads to more powerful analyses, however the number of locations in a typical neuroimage can preclude standard computation with explicitly spatial models. Here we contribute a Bayesian spatial regression model for group-level neuroimaging analyses. We induce regularization of spatially varying regression coefficient functions through Gaussian process priors. When combined with a simple nonstationary model for the error process, our prior hierarchy can lead to more data-adaptive smoothing than standard methods. We achieve computational tractability through Vecchia approximation of our prior which, critically, can be constructed for a wide class of spatial correlation functions and results in prior models that retain full spatial rank. We outline several ways to work with our model in practice and compare performance against standard vertex-wise analyses. Finally we illustrate our method in an analysis of cortical surface fMRI task contrast data from a large cohort of children enrolled in the Adolescent Brain Cognitive Development study.

1 Introduction

Modern large-scale neuroimaging studies collect massive amounts of data, often across thousands of patients, sometimes across several years (e.g., Akil et al., 2011; Smith and Nichols, 2018; Van Horn and Toga, 2009; Volkow et al., 2018). Typically these studies collect multiple structural and/or functional scans, with the aim to probe relationships between the images and patient-level characteristics. We focus here on an image-on-scalar regression treatment for this general framework, where patients’ images are taken to be the response, and covariates are individual-level scalars.

Since neuroimages are spatially referenced data, we can cast the image-on-scalar problem as a functional regression of the form,

$$y_i(\mathbf{s}) = \mathbf{x}_i^\top \boldsymbol{\beta}(\mathbf{s}) + \omega_i(\mathbf{s}) + \epsilon_i(\mathbf{s}). \quad (1)$$

In (1) we take $y_i(\mathbf{s})$ to be the imaging outcome for patient i ($i = 1, \dots, N$) at location $\mathbf{s} \in \mathbb{S}$, and coefficients of interest $\boldsymbol{\beta}(\cdot) : \mathbb{S} \rightarrow \mathbb{R}^P$ are treated as spatially varying. Further, we decompose the error into a sum of $\omega_i(\cdot)$ and $\epsilon_i(\cdot)$ terms, where $\omega_i(\cdot)$ reflects individual-level deviations from the mean with an assumed spatial structure, and $\epsilon_i(\cdot)$ is taken to be a white noise process. Many classical analysis methods in imaging can be cast within this framework. For example, in the typical group-level functional magnetic resonance imaging (fMRI) analysis, the $y_i(\cdot)$ might represent contrasts of parameter estimates from within-participant first level time series analyses, and $\mathbf{x}_i \in \mathbb{R}^P$ might include an intercept term along with any relevant covariate information. Often, univariate models are fit marginally to the data from each location \mathbf{s} in practice (e.g., Mumford and Nichols, 2009). This procedure tremendously simplifies estimation by avoiding modeling spatial correlations in $\boldsymbol{\beta}(\cdot)$ and $\omega_i(\cdot)$, but can lead to poorly calibrated inference (for example, see attempts to improve the power of tests derived from marginal ordinary least squares models by spatially pooling variance estimates in Nichols and Holmes 2002; Su et al. 2009; Wang et al. 2021).

For model (1) to make sense practically, the images must have reasonably comparable support in the spatial domain \mathbb{S} . Though it is still an area of active research, a tremendous amount of study has focused on methods to preprocess raw neuroimage data to help coregister the images across patients and data collection sites (e.g., Fischl et al., 1999a,b; Jenkinson et al., 2012; Reuter et al., 2010). In particular, certain neuroimage preprocessing tools compute state-of-the art cross-subject alignment of cortical features by first mapping each hemisphere of the cortex onto the surface of a sphere with minimal distortion (Fischl et al., 1999a,b). Fig. 1 gives an example of such a mapping. This procedure standardizes the spatial support for each hemisphere of cortex, and has already been shown to lead to reduced spatial signal contamination and result in more sensitive analyses (e.g., Brodoehl et al., 2020). Part of the gain from this methodology is due to the natural construction of a gray matter surface-based coordinate system which more accurately reflects the topology of primate cortex versus simple Euclidean distance in 3D space (Fischl et al., 1999a). Recently, within the statistical community, Mejia et al. (2020) highlighted this preprocessing pipeline by developing a cortical-surface-on-scalar regression model for task-based fMRI data. In their paper (Mejia et al., 2020), the authors propose a joint multi-subject spatio-temporal regression model, model their spatial regression coefficients with Gaussian random fields, and derive an integrated nested Laplace approximation routine for approximate Bayesian

inference. Per their data application, Mejia et al. develop their model primarily for analysis of multi-subject fMRI data where the number of subjects is not large (Mejia et al., 2020).

Such joint multi-subject spatio-temporal methods are not easily extensible to large-scale imaging studies. The number of spatial locations in a conventional neuroimage typically precludes Bayesian computation in most computing environments except by methods that either approximate (a) the spatial process by low-rank projection or downsampling, or that approximate (b) the posterior distribution with variational or Laplace family approximations (see e.g., Penny et al., 2005; Sidén et al., 2017; Mejia et al., 2020). In general, low-rank projection methods can tend to miss or over smooth local features in data (e.g., Stein et al., 2007), and both low-rank projection and variational approximation can commonly underestimate posterior variance (e.g., Wang and Titterton, 2005; Rasmussen and Quinonero-Candela, 2005). Integrated nested Laplace approximation, moreover, is thought to give accurate and scalable approximations within a wide class of posterior distributions (e.g., Rue et al., 2017), but its accuracy can sometimes suffer when model structure is complex (see e.g., Taylor and Diggle, 2014). Here, we expand on this body of work and show how a Bayesian model with a prior hierarchy related to that in Mejia et al. (2020) can permit estimation of coefficient functions that are realizations of a full-rank spatial process. To be able to extend our method to large-scale imaging studies we contribute a spatial regression model intended primarily for group-level analyses of data indexed by locations on the cortical surface. In the context of group-level fMRI studies, for example, our method could simply be “plugged in” at the classical second-stage analysis, with individual-level task contrast images taken to be the response. Our method can also be flexibly applied to analysis of cortical thickness outcomes, or other structural indicators. We model the probability law governing prior uncertainty in the functions $\beta(\cdot)$ and $\omega_i(\cdot)$ with Gaussian processes. Posterior computation is enabled by Vecchia approximation of the spatial process (Vecchia, 1988; Datta et al., 2016; Katzfuss and Guinness, 2021) and empirical Bayesian estimation of the spatial process hyperparameters.

Our model can be reasonably fit to the data from whole hemispheres of cortex using fast optimization or scalable Markov chain Monte Carlo (MCMC) routines without the need to downsample the original data. Additionally, we elaborate on an approximate working model and related Bayesian sampling scheme with computational complexity that scales almost independently of N , further allowing our method to be viable for application to large-scale neuroimaging studies. Model computation with MCMC permits posterior inference on the spatial extent of activation regions with simultaneous credible bands, which can facilitate spatial inference that is inherently adjusted for multiplicity. We show our method’s accuracy and sensitivity estimating the spatial coefficient functions in simulation. Finally, we use our method to analyze n-back task contrast data (z -statistic images) from the second annual

release of the Adolescent Brain Cognitive Development (ABCD) imaging collective data.

The body of this paper contains an elaboration of our spatial regression model hierarchy at the beginning of section 2. Sections 2.1, 2.2, and 2.3 develop schemas of using this model and a related working model in practice. Performance of these approaches is compared to standard vertex-wise univariate regression methods in section 3. We next illustrate use of our working model in a real fMRI task contrast data analysis in section 4. Section 5 concludes with a discussion of method limitations and possible extensions.

2 Methods

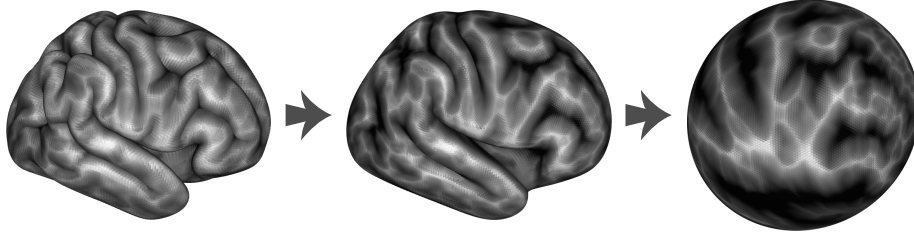


Figure 1: Example mapping of cortical surface coordinates onto a sphere. Left to right, the figure shows progressive inflation and warping of the right hemisphere of cortex. Gross anatomical features are highlighted to help visualize the mapping. This procedure was introduced to facilitate state-of-the-art cross-subject alignment of cortical features, but can also be leveraged into a mathematically convenient measure of geodesic distance along the cortical surface.

Throughout this work, we assume the single hemisphere, cortical surface-based, spherical coordinate system of (Fischl et al., 1999a). By isolating data from the cortical sheet we gain anatomical specificity and a better connection to the underlying neurobiology. As has been discussed by (Fischl et al., 1999a,b; Mejia et al., 2020), geodesic distances along the cortical surface are more meaningful than, say, simple Euclidean distances in the compact 3D volume. This is due to the fact that primate cortex is thought to be organized by function topographically (e.g., Silver and Kastner, 2009), and exhibits a folded structure in higher mammals to accommodate a larger cell body area (e.g., Cechetto and Topolovec, 2002; Jones and Peters, 2012).

We simplify notation by considering the left and right hemispheres of cortex as separate outcomes in separate analyses. Let \mathbb{S} denote the set of coordinates on a sphere with a known radius R , and let $\mathcal{S} \subset \mathbb{S}$ denote the set of vertices for a single hemisphere of cortex at which we have observed MRI data. For reference, the data in our application have all been mapped to a normalized template brain space with approximately 30,000 vertices in \mathcal{S} . In native patient brain space, \mathcal{S} may contain on the order of 150,000 vertices. For any

two $\mathbf{s}, \mathbf{s}' \in \mathbb{S}$, let $d(\mathbf{s}, \mathbf{s}')$ measure the great-circle distance between \mathbf{s} and \mathbf{s}' . Great-circle distance is sufficient for our purpose; more generally, however, \mathbb{S} might represent some topological surface, etc., and $d(\cdot, \cdot)$ any appropriate metric. Beginning from (1), we model the data likelihood as multivariate Gaussian with a particular error structure. We assume:

$$y_i(\mathbf{s}) \sim \mathcal{N}(\mathbf{x}_i^\top \boldsymbol{\beta}(\mathbf{s}) + \omega_i(\mathbf{s}), \sigma^2(\mathbf{s})), \quad i = 1, \dots, N, \text{ and } \mathbf{s} \in \mathcal{S}, \quad (2)$$

where $\mathcal{N}(\mu, \Sigma)$ denotes the Normal distribution with mean μ and variance Σ ; $\mathbf{x}_i \in \mathbb{R}^P$ are covariates; $\boldsymbol{\beta}(\cdot) : \mathbb{S} \rightarrow \mathbb{R}^P$ are the primary effects of interest; and $\omega_i(\cdot) : \mathbb{S} \rightarrow \mathbb{R}$ reflect individual-level deviations from $\mathbf{x}_i^\top \boldsymbol{\beta}(\cdot)$. Conditional on \mathbf{x}_i , $\boldsymbol{\beta}(\cdot)$, and $\omega_i(\cdot)$, we model the errors as a non-stationary white noise process with spatial variances denoted by $\sigma^2(\cdot) : \mathbb{S} \rightarrow \mathbb{R}_{>0}$. Given the nature of typical data in group-level functional or structural MR image analyses, this data-level model may be sufficient for a variety of studies.

Spatial dependence in our model arises entirely through our prior hierarchy on the effects $\boldsymbol{\beta}(\cdot)$ and $\omega_i(\cdot)$. Let $C_{\boldsymbol{\theta}}\{d(\mathbf{s}, \mathbf{s}')\}$ denote a positive definite stationary spatial correlation function defined on \mathbb{S} with parameter $\boldsymbol{\theta}$. For simplicity, we drop the subscript $\boldsymbol{\theta}$ throughout and use $C(\cdot)$ to represent a correlation function with implicit dependence on $\boldsymbol{\theta}$. We specify the prior distributions of each spatially varying coefficient function $\beta_j(\cdot)$ as mean zero Gaussian processes with marginal variances $\zeta_j^2 \tau^2$, i.e.,

$$\beta_j(\mathbf{s}) \sim \mathcal{GP}(0, \zeta_j^2 \tau^2 C\{d(\mathbf{s}, \mathbf{s}')\}), \quad j = 0, \dots, P-1. \quad (3)$$

This class of prior for functional regression coefficients has been adopted by Gelfand et al. (2003) for general spatial regression problems. We write the coefficient processes this way without loss of generality: while zero mean processes are reasonable in our application (where outcomes are task contrast z -statistic images, see section 4), data from other imaging modalities may require centering at the global mean for zero mean priors to make the most sense.

We treat the individual-level deviations $\omega_i(\cdot)$ as spatially varying random effects with mean zero and marginal variance τ^2 ,

$$\omega_i(\mathbf{s}) \sim \mathcal{GP}(0, \tau^2 C\{d(\mathbf{s}, \mathbf{s}')\}). \quad (4)$$

Next, we specify a relatively simple nonstationary process for the error precisions,

$$\sigma^{-2}(\mathbf{s}) \mid \xi \stackrel{\text{iid}}{\sim} \text{Gamma}(1/2, \xi), \quad \xi \sim \text{Gamma}(1/2, 1), \quad (5)$$

using the shape-rate parameterization of the Gamma distribution. To complete our model

hierarchy, we place weakly informative priors on the remaining spatial variance components,

$$\tau^{-2} \sim \text{Gamma}(1, 1/2), \quad \zeta_j^{-2} \stackrel{\text{iid}}{\sim} \text{Gamma}(1, 1/2). \quad (6)$$

As noted above, the correlation function $C(\cdot)$ can in general be any positive definite kernel function defined so that $C(0) = 1$ and $C(\alpha) \leq 1$ for all $\alpha > 0$. Given the substantial history of Gaussian smoothing in applied MRI analysis, we will work chiefly with the two parameter exponential radial basis function,

$$C(\alpha) = \exp(-\psi|\alpha|^\nu), \quad \boldsymbol{\theta} = (\psi, \nu)^\top, \quad \psi > 0, \nu \in (0, 2], \quad (7)$$

which is stationary, isotropic, and synonymous with the Gaussian kernel when $\nu = 2$. In (7), ψ is sometimes called the bandwidth or inverse length-scale parameter and controls how rapidly the correlations decay, and ν is the kernel exponent or smoothness parameter. Alternative correlation functions could be used just as easily. We will discuss one data-driven way the correlation function might be selected in practice in section 2.5; the same method can also be used to estimate the correlation parameters $\boldsymbol{\theta}$ for a given functional family.

2.1 Conditional Model

We outline two ways of working with model (1) in our setting, and also study the relative behavior of an approximate working model with connections to the standard vertex-wise analysis framework. The regression model that we have outlined is difficult to work with without simplification for two reasons. The first and perhaps most obvious reason is the dimension of the parameter space. Computational strategies for spatial modeling typically involve decomposition of a dense spatial covariance matrix. In our case, naive decomposition of the joint covariance of the $\beta_j(\cdot)$ and the $\omega_i(\cdot)$ would be an $\mathcal{O}(M^3(N+P)^3)$ operation, where M is number of vertices in \mathcal{S} , and N and P are the sample size and number of regression predictors, respectively. In Bayesian sampling algorithms, this decomposition often needs to be recomputed for each sample, which is prohibitively expensive in our setting. The other difficulty working with the model as written is that decomposing the error structure into the sum of two spatially varying terms (i.e., the $\omega_i(\cdot)$ and the $\epsilon_i(\cdot)$) renders the whole model at best weakly identifiable.

As we lay out in greater detail in the Supporting Information, we overcome the first difficulty by using a conditional independence approximation to the model parameters' spatial covariance, inducing sparsity in the parameters' spatial precision. This type of approximation can greatly reduce the computational burden while retaining a covariance

structure with full spatial rank, leading to high accuracy and scalability (e.g., Datta et al., 2016; Finley et al., 2019). We overcome the second difficulty in several different ways, and we first introduce what we term the “conditional” approach to working with our model. To explain our conditional estimation strategy, we first observe that if we knew the correct $\omega_i(\cdot)$ the remaining terms in the model would be relatively easy to estimate. For this approach, our strategy will be first to obtain an approximate maximum a posteriori estimate of the $\omega_i(\cdot)$, and second to condition on those estimates, sampling the other model parameters in an Empirically Bayesian way. To obtain these estimates, we work with an approximate model that considers $\sigma^2(\mathbf{s}) \equiv \sigma^2$ constant over all vertices in \mathcal{S} , and alternate conditional maximization of $\beta(\cdot)$ and the $\omega_i(\cdot)$ until convergence. Once we have obtained our estimate of the $\omega_i(\cdot)$ in this way we simply subtract the $\omega_i(\cdot)$ from the $y_i(\cdot)$, and switch to an efficient Bayesian sampling algorithm for the remaining parameters in the model.

2.2 Marginal Model

Alternatively, since the individual deviations $\omega_i(\cdot)$ are not typically of direct interest, we can first integrate them out, leading to a marginal model with respect to the $\beta_j(\cdot)$, $\sigma^2(\cdot)$, etc. Marginalizing out the $\omega_i(\cdot)$ is relatively straightforward given the conjugacy in our model hierarchy. Marginalization leads to the equivalency,

$$y_i(\mathbf{s}) = \mathbf{x}_i^\top \beta(\mathbf{s}) + \epsilon_i^*(\mathbf{s}), \quad \epsilon_i^*(\mathbf{s}) \sim \mathcal{GP}(0, H\{d(\mathbf{s}, \mathbf{s}')\}), \quad (8)$$

when $H\{d(\mathbf{s}, \mathbf{s}')\} = \tau^2 C\{d(\mathbf{s}, \mathbf{s}')\} + \sigma^2(\mathbf{s}) \mathbb{1}\{d(\mathbf{s}, \mathbf{s}') = 0\}$, and $\mathbb{1}(\mathcal{A})$ is the event indicator function ($\mathbb{1}(\mathcal{A}) = 1$ if event \mathcal{A} occurs, and 0 otherwise). A computational approach to working with model (8) can then follow by additional application of a conditional independence approximation (Datta et al., 2016; Finley et al., 2019) to the covariance of the $\epsilon_i^*(\cdot)$. In the Supporting Information, we outline a means of computing with model (8) based on estimating θ , τ^2 , and $\sigma^2(\cdot)$ in an Empirically Bayesian way. Briefly, we take a two stage approach to computation, first obtaining approximate (up to optimization tolerance) maximum a posteriori estimates of $\beta(\cdot)$, θ , τ^2 , and $\sigma^2(\cdot)$. Second, we fix the covariance parameters θ , τ^2 , and $\sigma^2(\cdot)$ at their approximate posterior modes and switch to an efficient MCMC routine to sample from the conditional posterior of $\beta(\cdot)$.

2.3 Working Model

We also introduce a third, working model as a way to obtain approximate inference on the $\beta_j(\cdot)$. In general, including the $\omega_i(\cdot)$ as a separate correlated error component will not influence standard estimators of the center of the posterior of the $\beta_j(\cdot)$, such as the posterior mean. If out of sample prediction of imaging outcomes is not a goal of the analysis,

then the primary reason to include a spatially correlated error component is to reduce the posterior variance of the $\beta_j(\cdot)$. In a large data setting, the gain in efficiency from including a correlated error component can be minimal to negligible. A natural question, then is if we replace the likelihood in (2) with the approximation,

$$y_i(\mathbf{s}) = \mathbf{x}_i^\top \boldsymbol{\beta}^w(\mathbf{s}) + \epsilon_i^w(\mathbf{s}), \quad \epsilon_i^w(\mathbf{s}) \sim \mathcal{N}(0, \sigma^2(\mathbf{s})), \quad (9)$$

and keep the prior structure on the $\beta_j^w(\cdot)$ and $\sigma^2(\cdot)$ is the same as in (3) and (5) above, how well does the resulting model perform? We term this approximation our “working” model, and note that it can be viewed as a generalization of the standard vertex-wise GLM analysis paradigm in a spatial Bayesian context. The model implied by fitting vertex-wise marginal GLMs is a limiting case of our working model as $\tau^2 \rightarrow \infty$ for select choices of the correlation function, $C(\alpha) = \mathbb{1}(\alpha = 0)$, and (improper) prior on the $\sigma^{-2}(\cdot) \sim \text{Gamma}(1, 0)$. Considering comparisons among our suite of methods, we will show in simulation that for moderate to large sample sizes, the posterior of the $\beta_j^w(\cdot)$ for our working model is quite similar to that of the $\beta_j(\cdot)$ from either our conditional or marginal models.

2.4 Posterior computation

The Supporting Information provides a detailed description of our approach to posterior computation. Space does not permit us to elaborate here. Very briefly, we follow work on “Nearest Neighbor Gaussian Processes” (Datta et al., 2016; Finley et al., 2019) to develop sparse Vecchia-type approximations to the inverses of key spatial covariance matrices. These approximations require some definition of a spatial neighborhood within which the spatial precisions are non-sparse. For both our simulations and applied analysis, we have used discs with 8 mm radii to constitute these neighborhoods. Sensitivity analyses over this choice are presented in the Supporting Information. We combine Vecchia approximation with a quasi-Newton Hamiltonian Monte Carlo (HMC) algorithm to sample from the conditional posterior of the regression coefficients supported on the fixed spatial domain \mathcal{S} . Each gradient step of our HMC algorithm is scaled by a sparse preconditioning matrix related to the prior precision of the regression parameters on \mathcal{S} .

The algorithm we have briefly outlined above can be used for efficient posterior computation in very large data sets. In fact, given sufficient statistics that can be computed with a single pass through the outcome images, all of the parameter updates in our working model can be performed without reference to the original data. This leads to computational time complexity that, save for an initial data streaming step, is independent of N . In large data regimes the advantage of this is obvious. A common applied fMRI use-case when working with task contrast images is to use a simple set of predictors: practitioners often

fit an intercept-only model, or perhaps additionally control for select covariates like age and sex. We benchmarked our working model software for these use cases, analyzing right hemisphere task contrast data from over 3,000 participants ($\approx 30,000$ vertices; see section 4 for a more in-depth analysis). Streaming the images typically took around 100 ms or less per image (CIFTI/NIFTI-2 file format: <https://www.nitrc.org/projects/cifti/>). After streaming, analysis with HMC took around 3.3 min per 1,000 iterations for the intercept-only model, or around 18.8 min per 1,000 iterations for the three predictor model (intercept, age, and sex). Each analysis used less than 300 Mb of free RAM, demonstrating the scalability of our approach. We ran this comparison on a Dell PowerEdge R440 server with Intel[®] Xeon[®] Gold 6230 processors (2.1 GHz), limiting our processes to use eight cores each.

2.5 Estimation of θ and $C(\cdot)$

Commonly used methods to estimate the spatial correlation function include variogram or covariogram estimation (e.g., Armstrong, 1984; Cressie and Glonek, 1984), and maximum marginal likelihood methods (e.g., Mardia and Marshall, 1984). These methods can also be used to select the correlation function itself by taking, for example, the correlation function resulting in the best fit to the variogram or the highest marginal likelihood. Here, we have used a maximum marginal likelihood-based approach for a surrogate model to estimate the correlation function and corresponding parameters in the spirit of Empirical Bayes. The Supporting Information provides a full description of this selection method for interested readers. In our analysis of the ABCD study data (section 4), we estimated $\theta = (0.17, 1.38)^T$, which corresponds to a sub-Gaussian correlation function with 5.57 mm full-width-at-half-maximum (FWHMs).

In addition to likelihood-based or (co)variogram estimation, experience can guide practitioners selecting $C(\cdot)$ and θ to a large extent. In applied imaging it is common to apply a Gaussian smoothing kernel to data prior to analyses. In part, the goal of this practice is to approximate a full spatial model for effects of interest (e.g., Thirion, 2016). Commonly applied smoothing kernels are specified by their FWHMs, which are often chosen to be within a 4–12 mm range (e.g., Mikl et al., 2008). A 6 mm FWHM Gaussian kernel, for example, is nominally equivalent to a radial basis correlation function (7) with bandwidth parameter $\psi = 0.077$ and exponent parameter $\nu = 2$. In our setting with moderate to large N , we often find that posterior inference is not be overly sensitive to the choice of θ .

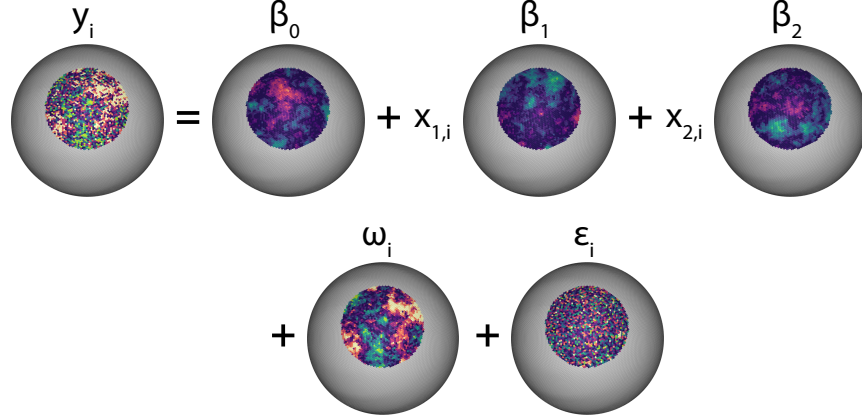


Figure 2: Simulation design. Data were simulated over a disc of 2,000 vertices on a spherical surface. Effects of interest β_j , $j = 0, 1, 2$ were simulated as hard-thresholded Gaussian fields each with approximate 30% sparsity. Error terms ω_i and ϵ_i were drawn from larger variance spatial processes and dominate the spatial signals of interest such that the spatial signal-to-noise ratio was controlled to be approximately 0.04. We have enhanced the contrast of the β_j images for visual clarity. See online version for color figures.

3 Simulation Study

Our goal in simulation was to compare the performance of our two methods for estimating our model against our “working model” and the standard vertex-wise marginal linear model approach. In all cases, data were simulated from model (2) on a disc of 2,000 vertices on the cortical surface. We designed our simulation to mimic spatial smoothness and signal-to-noise ratios estimated from real data. Fig. 2 illustrates this approach. For each simulated data set, we generated spatially correlated and sparse $\beta_j = [\beta_j(\mathbf{s})]_{\mathbf{s} \in \mathcal{S}}$, $j = 0, 1, 2$, by hard thresholding draws from independent Gaussian processes with 6 mm FWHM exponential correlation functions. Below, we will also use β without the subscript to refer to the vector of concatenated random fields $\beta = (\beta_0^\top, \dots, \beta_p^\top)^\top$

We set the marginal variance parameter of each Gaussian field drawn this way to 0.04 and thresholded the result at 0.08 so that each β_j would be approximately 30% sparse on average. This level of sparsity roughly matches pseudo-sparsity in the real data we analyze in section 4: applying standard vertex-wise GLM methods with a Bonferroni correction-based p -value threshold to these data resulted in significant findings over about 70% of the cortical surface. Since our prior model in (3) is non-sparse, simulating the β_j in this way actually reflects a setting with slight model misspecification. It is important to consider such a setting, however, in order to evaluate models using measures of inferential accuracy. We treated the field β_0 as a spatially varying intercept parameter and paired β_1 and β_2

with covariates: for subject $i = 1, \dots, N$, corresponding covariates $(x_{1,i}, x_{2,i})^\top$ were drawn jointly from a multivariate Gaussian distribution with mean zero, unit marginal variance, and correlation parameter 0.5.

In each simulation, we also generated the subject-level deviations $\omega_i = [\omega_i(\mathbf{s})]_{\mathbf{s} \in \mathcal{S}}$ as draws from independent Gaussian processes with 6 mm FWHM exponential correlation functions. Again to mirror estimates from the real data, we set the marginal variance of each ω_i to 1.75. In a similar vein, we drew each $\epsilon_i = [\epsilon_i(\mathbf{s})]_{\mathbf{s} \in \mathcal{S}}$ following a white-noise process with spatially constant variance 1.25. Under the above parameter settings, we controlled the spatial signal-to-noise ratio to be approximately 0.04 (or equivalently, the spatial R^2 was controlled to be approximately 3.8%). As can be seen from Fig. 2, the error terms ω_i and ϵ_i largely dominate the spatial signal. Within this regime, we studied the behavior of our various comparison methods for increasing sample size, replicating the simulation 50 times per sample size.

In all cases, we then fit our suite of three methods to compare against the standard vertex-wise GLM conditioning on the true correlation parameters (or smoothing the outcome images with exactly a 6 mm FWHM exponential kernel in the case of the standard method). For comparison, we give the standard vertex-wise analysis paradigm a Bayesian treatment by replacing our priors on the $\beta_j(\cdot)$ and $\sigma^2(\cdot)$ with independent Jeffreys priors (as alluded to in section 2.3). Since the full conditional posterior distributions of the resulting model parameters are quite easy to sample from we fit the vertex-wise models using Gibbs sampling. Working with the model in this fashion allowed us to compare the standard vertex-wise analysis to our proposed models in terms of full posterior inference. Namely, we used posterior credible bands as a way to summarize the joint uncertainty in the $\beta_j(\cdot)$ over all vertices simultaneously. In a spatial modeling context, posterior credible bands are a natural, fully Bayesian approach to inference, and can be easily estimated from MCMC samples (see e.g., Ruppert et al., 2003). Since credible bands reflect posterior probability statements about the joint behavior of the $\beta_j(\cdot)$ for all spatial locations, inference derived from them is inherently multiplicity-adjusted.

3.1 Results of simulation comparisons

Table 1 summarizes the results of our simulation for increasing sample size. For each method in the table, we report scaled absolute bias and variance as well as sensitivity and specificity rates ($True +$ and $True -$, respectively; expressed as percentages. Since the scale of each $\beta_j(\cdot)$ is the same for all j in simulation we report absolute bias and variance as averages over the entire parameter vector β , so that the values in Table 1 can be interpreted as the scaled expected point-wise bias or marginal variance of each $\beta_j(\mathbf{s})$. For example, the absolute

Table 1: Simulation results focusing on parameter estimation (absolute bias and variance) and inferential accuracy (true positive and true negative rates). Results are reported as mean (standard error). Absolute bias and variance have been scaled by a factor of 10^3 to facilitate comparison; true positive and negative rates (sensitivity and specificity, respectively) are expressed as percentages.

<i>Method</i>	<i>N</i>	$ Bias $	<i>Variance</i>	<i>True +</i>	<i>True -</i>
Conditional	20	249.8 (3.9)	19.4 (0.4)	14.7 (0.7)	91.5 (0.4)
Marginal	20	178.1 (2.4)	17.5 (0.2)	4.0 (0.5)	98.5 (0.3)
Working Model	20	264.9 (4.4)	59.3 (1.8)	1.6 (0.1)	99.5 (0.1)
Vertex-wise GLM	20	228.1 (4.1)	77.7 (2.6)	0.0 (—)	100.0 (—)
Conditional	100	121.2 (1.5)	5.9 (<0.1)	26.2 (0.6)	95.1 (0.3)
Marginal	100	111.0 (1.3)	10.0 (<0.1)	7.2 (0.5)	99.6 (0.1)
Working Model	100	122.9 (1.5)	14.6 (0.2)	6.8 (0.3)	99.8 (<0.1)
Vertex-wise GLM	100	123.0 (1.3)	13.7 (0.2)	2.8 (0.4)	99.8 (<0.1)
Conditional	500	61.1 (0.4)	2.1 (<0.1)	53.6 (0.6)	98.0 (0.1)
Marginal	500	61.3 (0.4)	4.2 (<0.1)	27.5 (0.7)	99.9 (<0.1)
Working Model	500	61.2 (0.4)	4.4 (<0.1)	29.7 (0.5)	99.9 (<0.1)
Vertex-wise GLM	500	89.8 (0.3)	2.7 (<0.1)	29.3 (1.0)	96.2 (0.2)

bias column reports $10^3 \sum_{j,s} |\hat{\beta}_j(\mathbf{s}) - \beta_j(\mathbf{s})| / (3 \times 2,000)$, where $\hat{\beta}_j(\cdot)$ is the posterior mean estimate for a given method (three predictors; 2,000 spatial locations; scaled by a factor of 10^3 to enhance the clarity of the table). We constructed example inferential decisions based on 80% simultaneous credible bands. The 80% credibility threshold was chosen to represent a selection that might reasonably be applied in practice rather than by optimizing any kind of inferential criterion. In Table 1, the *True +* column corresponds to the average percentage of cases where the true $\beta_j(\mathbf{s}) \neq 0$ and the corresponding credible band does not include zero. Similarly, the *True -* column reports the average percentage of cases $\beta_j(\mathbf{s}) = 0$ and the corresponding credible band covers zero.

The most immediate result of our simulations is that the marginal method of estimating our model typically leads to the most accurate posterior mean estimate of β in the mean squared error sense. For all methods under consideration, the point-wise bias dominates the point-wise variance across all simulation settings. At large sample size we note that both the marginal and conditional methods of estimating our model as well as our working model tend to produce very similar estimates and results. This pattern is explored further in Fig. 3, which summarizes the similarity of the full posterior distribution of β , as estimated with our suite of methods. It is clear from the figure that differences in estimation between methods decay as the sample size increases. Interestingly, at small sample sizes, our conditional and working model methods have higher absolute bias than the vertex-wise

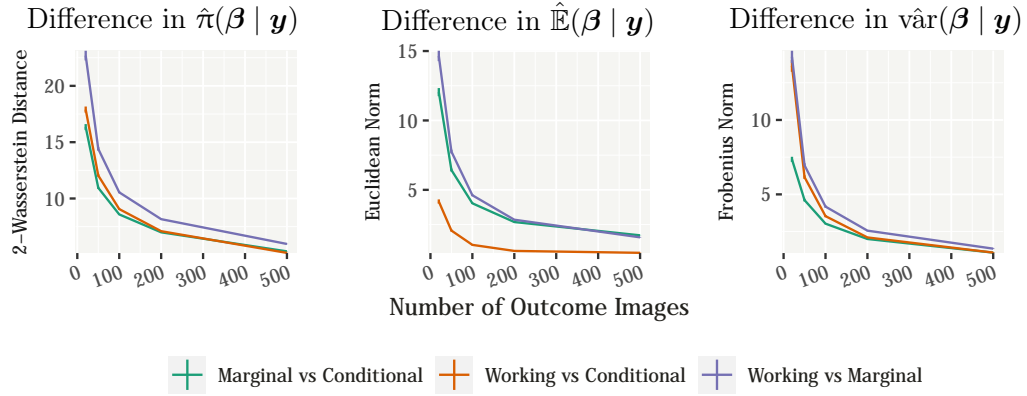


Figure 3: Comparison of the posterior distributions of β across our suite of methods. In the left panel, 2-Wasserstein distance was computed using a Gaussian approximation to the posterior, derived from MCMC samples. The center and right panels of the figure show the similarity in the posterior mean and variance of β , summarized as the Euclidean and Frobenius norms of the differences, respectively. Error bars are minimally visible, but show ± 1 simulation standard error. See online version for color figures.

GLM, but quickly overtake the vertex-wise method as the sample size increases. Absolute bias does not decrease with increasing N as rapidly for the vertex-wise GLM as for our suite of methods. The other major result indicated by our simulations is that, using simultaneous credible bands for inference, the conditional method of estimating our model is the most powerful or sensitive among our methods under comparison. The sensitivity of this method, however, is modestly lacking compared to our marginal and working model methods, which make virtually no false positive errors even at smaller sample sizes.

This pattern of results can be somewhat difficult to summarize. Based on this simulation, we cannot uniformly recommend any one method without knowledge of the goals of the intended analysis. If estimation of β is of primary concern, then we would generally recommend our marginal method if the sample size is small, or any of our suite of methods at larger sample sizes. If inference is of primary concern, we might recommend our conditional method, for example, for its high sensitivity. Alternatively, we might also recommend either our marginal or working methods for their rather low false positive to true positive ratio.

4 Data Analysis

4.1 Description of the data and model terms

To illustrate use of our methodology, we applied our working model to analyze n-back task contrast data from the ABCD study, release 2.0.1 (Jernigan et al., 2019). A brief comparison of estimation differences between our working, conditional, and marginal model variants is available for these data in the Supporting Information. The ABCD study is the product of a large collaborative effort to study longitudinal changes in the developing brain through childhood and adolescence, and to track biological and environmental correlates of development (Feldstein-Ewing and Luciana, 2018). Data collection and processing has been harmonized across 21 research sites in the continental United States. At the time of writing, the study has collected baseline environmental, behavioral, genetic, and neuroimage data from over 11,800 children between the ages of 9–10 years. Longitudinal data has been collected at six month intervals for a subset of children in the study; already over 3,600 children have been enrolled for over 2.5 years. Details regarding study design and recruitment (Garavan et al., 2018), neurocognitive assessment (Luciana et al., 2018), and neuroimage acquisition (Casey et al., 2018) are available in published literature. The ABCD data repository grows and changes over time. The ABCD data used in this report came from NDA study 2573. DOIs can be found at <https://nda.nih.gov/study.html?id=721>. Preprocessing of the fMRI task data was accomplished through use of a published standardized pipeline (see Sripada et al., 2021, “Supplemental FMRIPrep Methods”).

We focus our analysis on the relationships between task-related activation and individual-level task accuracy, which has been studied previously (see e.g., Li et al., 2021, for a recent article). In concert, our analysis controls for various child-level characteristics and family-level demographic information. We took 2- vs 0-back task contrast data (z -statistic scale) as our primary outcome and modeled it as a function of 2-back task accuracy; child fluid intelligence; child age (months); child gender (binary); parental education (five levels); parental marital status (binary); and family income (three levels). We included first-order interactions between child gender and parental education; child age and parental education; child age and child gender; child age and 2-back accuracy; and child gender and 2-back accuracy. For interpretive purposes, we centered continuous covariates in the analysis on their respective in-sample means, and we treated the in-sample modal demographic categories as baseline (female child from a married household, at least one parent with a post graduate degree, and household income greater than \$100,000 USD/year). The intercept parameters in our spatial regression can be interpreted thus as the expected task contrast image for a typical in-sample female child of average fluid intelligence that scored 80% correct on the

2-back task condition.

Covariates were chosen largely on the basis of known associations with general n-back task accuracy (Pelegrina et al., 2015). In addition, we performed sets of exploratory analyses in the classic vertex-wise framework without any spatial smoothing (not shown). These analyses served to help us visualize and understand several important aspects of the data. Interested readers can find a more comprehensive report of non-intercept regression effects in our Supporting Information.

4.2 Summary of primary results

The primary results of our analysis are presented in Fig. 4. We consolidate the output by focusing on results in the right hemisphere, and we note that in general results in the left hemisphere are highly symmetric. In particular, Fig. 4 shows the posterior mean estimate of our model intercept parameters (β_0) and also gives a region of interest level summary of this term. Regions of interest were taken from the Gordon 2016 cortical surface parcellation atlas, which was created in part from resting state functional connectivity maps and naturally groups brain regions within a network community structure (Gordon et al., 2016). The atlas delimits 172 brain regions in the right hemisphere (161 in the left), each grouped within one of 13 functional network communities.

To summarize our model intercept by brain region, we fit a series of mixed effect models to MCMC samples of β_0 , taking advantage of the Gordon atlas’s grouped structure. We used this modeling strategy to obtain region-level averages of our spatial intercept parameters, where each region-level average is shrunk towards its network community mean. By repeatedly fitting this model to each sample of β_0 , we obtain Bayesian point and interval estimates for the region-level averages. The bottom panel of Fig. 4 displays point and multiple comparisons consistent 95% interval estimates for a subset of regions in the Gordon 2016 atlas. Although we model and adjust the intervals based on all 172 regions in the atlas, we only show the region-level estimates for regions belonging to communities: Cingulo-Opercular network, Default mode network, Dorsal attention network, Fronto-Parietal network, and “None” (see Fig. 4). Results of this analysis show that the largest activations occur in regions associated with the Dorsal attention, Fronto-Parietal, and Cingulo-Opercular networks, with a handful of regions associated with the Default mode network also showing significant activations. Similar conclusions were reached by (Casey et al., 2018) in a smaller, preliminary subset of these data ($N = 517$). Data from another large collective imaging study also support similar results in adults aged 22–37 years ($N = 949$; Li et al., 2021).

Fig. 5a depicts example spatial inference on the intercept parameters in the right hemisphere, thresholding at what we might consider a small to medium effect size. In the

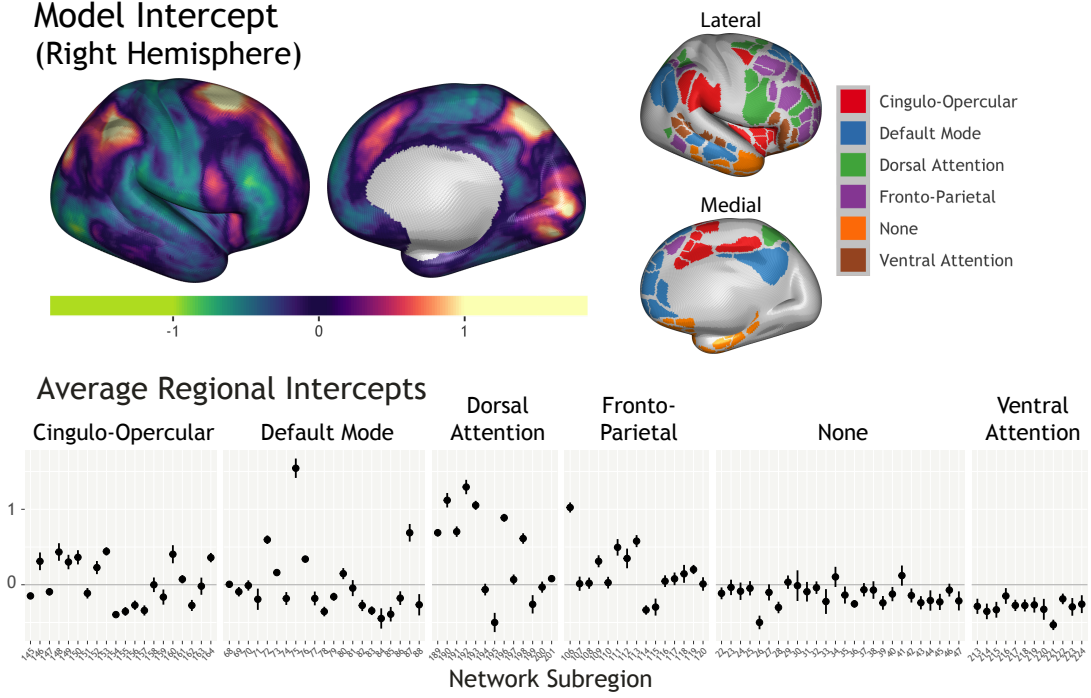


Figure 4: Model intercept coefficients summary. The upper left corner of the figure shows the posterior mean estimate of the intercept, which can be interpreted as a one-sample t -test for the 2- vs 0-back contrast, controlling for demographic information (see the main text for details). Forest plots in the bottom row of the figure summarize the intercept parameters in terms of region-level averages, with regions taken from the Gordon 2016 cortical surface parcellation (Gordon et al., 2016). Error bars in the forest plots correspond to fully Bayesian 95% intervals that have been widened to be multiple-comparisons consistent (Bonferroni adjustment). The upper right panel of the figure shows the brain regions represented on the x -axis in the bottom row forest plots. Region numbers correspond to the Freesurfer labels for the Gordon parcellation. Left to right the region labels read, Cingulo-Opercular: 145–164; Default Mode: 68–88; Dorsal Attention: 189–201; Fronto-Parietal: 106–120; None: 22–47; Ventral Attention: 213–224. See online version for color figures.

figure, colored regions denote areas where the posterior mean estimate of $|\beta_0(\mathbf{s})|$ is greater than 0.4 (see online version for color figures). Since we are modeling z -statistic outcomes, $\beta_0(\mathbf{s}) > 0.4$ can be interpreted to mean that roughly 2 out of every 3 “average” children in our sample would show task-related activation at location \mathbf{s} (versus 1 in 3 showing deactivation; the statement can be reversed for $\beta_0(\mathbf{s}) < 0.4$). Regions of darker color in Fig. 5a mark areas where our analysis suggests the probability that $|\beta_0(\mathbf{s})| > 0.4$ is greater than or equal to 80% simultaneously for all vertices \mathbf{s} within those areas. This interpretation is similar to the notion of “upper confidence sets” from (Bowring et al., 2021). Here, as in in Section 3, we use posterior credible bands (see e.g., Ruppert et al., 2003) to create

these inferential summaries. Model residual standard deviations for the right hemisphere is shown in Fig. 5b. In general, areas with the highest residual variance overlap with areas activated in the 2- vs 0-back contrast (confer from Figs. 4 and 5b). This result indicates substantial variability in individual responses in these regions. Overall, our fitted model explained about 6.2% of the total variance in the task contrast images.

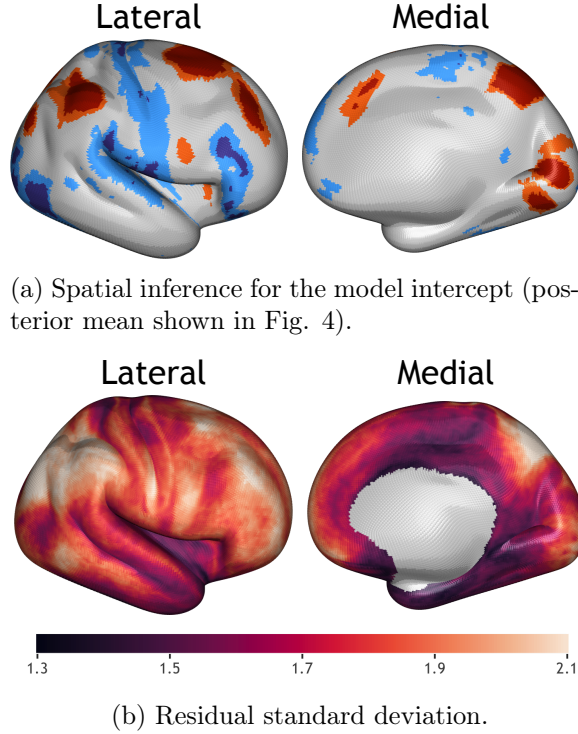


Figure 5: (5a) Model intercept for the right hemisphere: example signed discoveries using an 80% posterior simultaneous credible band to infer locations where $|\beta_0(\cdot)| > 0.4$. Red regions correspond to functional activations and blue regions correspond to deactivations. Darker colors indicate regions of simultaneous posterior confidence that $|\beta_0(\mathbf{s})|$ is greater than 0.4 for all vertices \mathbf{s} in those regions. Lighter colors can be thought of as reflecting the spatial uncertainty in that claim of posterior credibility. (5b) Residual standard deviation for the right hemisphere. Areas of high residual variation generally overlap with activation areas in the 2- vs 0-back contrast (confer with Fig. 4). See online version for color figures.

4.3 Goodness-of-fit evaluation

Finally, we assess the fit of our model using posterior predictive simulation (Rubin, 1984; Gelman et al., 1996) and analysis of model residuals. Selected results of these comparisons are presented in Fig. 6. In the figure, we summarize the extent of discrepancy between the observed data and posterior predictions the model would make for replicated data. To do

this, we again leveraged the Gordon 2016 cortical surface parcellation Gordon et al. (2016) and computed test descriptive statistics across subjects within each brain region, comparing against the same statistics computed over synthetic data of the same size simulated from our fitted model. We explored the discrepancies in the predictive and empirical data distributions based on measures of central tendency, spread, and several quantiles. Absolute differences in the empirical values and the posterior predictive mean value are shown in Fig. 6 for each brain region and for three such test statistics. To give a sense of scale, in the figure the largest regional difference is < 0.2 (10th Quantile panel), whereas the range of the data is approximately -13.7 to 17.1 . In general, we found that discrepancies between the empirical and predictive distributions were extremely low for test statistics that summarize features of the central bulk of the distributions. Features in the very tails of the empirical distribution were less well captured in the predictive distribution, as might be expected for a Gaussian likelihood model (not shown). In Fig. 6, we also summarize goodness-of-fit by comparing standardized residual histograms for each brain region. In the lower panel of Fig. 6, we ranked each brain region by their discrepancy with a normal model and show residual histograms for the best, median, and worst-case regions. In general, we again see evidence of excellent model fit throughout the central bulk of the data. Interestingly, region 192 (worst-case fit) contained the highest overall mean parameter estimate within the Dorsal-Attention network community for both the intercept and linear 2-back accuracy term (Fig. 4; as in Fig. 4, “192” corresponds to the Freesurfer label for the Gordon atlas region; see <https://surfer.nmr.mgh.harvard.edu/fswiki>). This result may indicate, for example, that while the (relatively simple) model we have used for 2-back accuracy provides a reasonable fit to the task contrast data across most of the right hemisphere, it may fail to perfectly encapsulate the complex task-related activation patterns in this sample.

5 Discussion

Here we propose a Bayesian spatial model for group-level image-on-scalar regression analyses, and illustrate several ways to consider working with the model in practice. We also show how the spatial Gaussian process prior formulation and related approximation through conditional independence methods can enable flexible and reasonably efficient computation with MCMC. Critically, our approach allows us to work with full-rank spatial processes numerically, and does not rely on lossy compression schemes like down-sampling or low-rank projection, which can be dissatisfying in practice (e.g., Stein et al., 2007). We have shown in simulation that our strategy can improve on the standard analysis stream in terms of finite sample bias, sensitivity, and specificity. We have also shown that an approximate working model produces similar inference on the spatially varying coefficients $\beta(\cdot)$ in set-

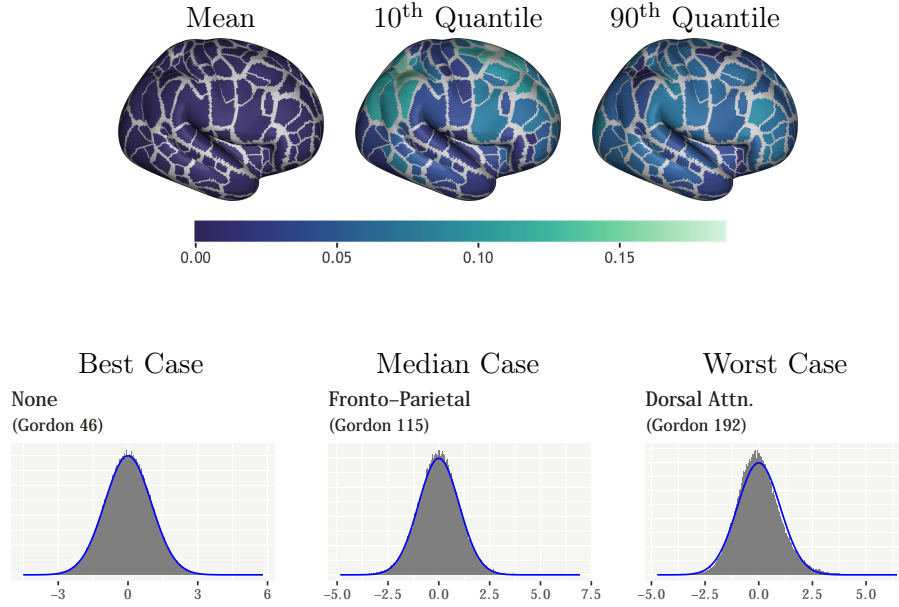


Figure 6: Goodness of fit checking. (*Top*) Absolute differences in the observed and mean posterior predictive value for three different test statistics computed across all subjects and vertices for each brain region in the Gordon 2016 parcellation (Gordon et al., 2016). Test statistics shown are the regional mean and 10th and 90th quantiles. In the figure, predictive checking is homogeneous within each brain region; the gray shows a boundary area not assigned to any particular region. (*Bottom*) Histograms of standardized residuals from three different brain regions. Blue lines show the fit of model at the posterior mean. The three different regions chosen show the best, the median, and the worst-case scenarios for the model’s goodness-of-fit in these areas. See online version for color figures.

tings with moderate to large N . Our working model is relatively easy to compute with, and can be thought of as a generalization of the standard analysis stream. Finally, we illustrate use of our method on task (n-back) contrast data from the Adolescent Brain Cognitive Development study.

With the exception of a white-noise component our model error process, we express our model as a sum of terms assigned stationary spatial priors in section 2. In general, spatial stationarity is not considered a realistic assumption for imaging data (see e.g., Woolrich et al., 2004; Aja-Fernández et al., 2015). Although we use stationary priors throughout for simplicity, in practice, given the data the posterior distribution of our model parameters can still reflect non-stationary processes. In fact Fig. 4 illustrates clear posterior mean field non-stationarity. In particular, the posterior mean of our model intercept and linear 2-back accuracy rate coefficients suggest obvious mean-field non-stationarity. Moreover, since our model on the white-noise process is inherently non-stationary, our prior hierarchy can lead to

more data-adaptive smoothing in the regression coefficients compared to standard analysis streams where stationary spatial smoothing is applied, at some level, to the data.

As we alluded to in Section 4.1, it may be of interest to build extensions to our method to incorporate additional variance components for more complex or specific study designs. Such an extension might correspond, for example, to the addition of random family effects in analyses of the greater ABCD study sample. While our present model is technically capable of estimating such effects by pooling the corresponding ζ_j^2 across related terms, including a large number of random spatial effects in the analysis can be extremely demanding computationally. One workaround might be to omit modeling spatial correlation structures for these terms, and treat them as pure nuisance parameters. At the time of writing, we have not yet studied the practical consequences of doing so.

Acknowledgements

The authors would like to thank Mike Angstadt, Dr. Chandra Sripada, and Dr. Mary Heitzeg, who oversaw preprocessing of the fMRI data we used to illustrate our methods, and who provided helpful feedback on our work. This work was partially supported by NIH R01 DA048993 (Kang and Johnson).

Supporting information

Appendices including Tables and Figures referenced in Sections 2 and 4 are provided below. Software for our methods is available online at <https://github.com/asw221/gourd>.

A Posterior computation

We outline our general approach to computation using the working model in the main text as a running example, since this variant is the easiest to work with. Posterior computation with the conditional and marginal models can be accomplished in very similar fashion.

Since we typically work on a fixed spatial domain \mathcal{S} , let β_j (dropping the superscript w for simplicity) denote the random field $[\beta_j^w(\mathbf{s})]_{\mathbf{s} \in \mathcal{S}}$ for $j = 0, \dots, P-1$, and let $\beta = (\beta_0^\top, \dots, \beta_{P-1}^\top)^\top$. Let $\mathbf{C} = [C\{d(\mathbf{s}, \mathbf{s}')\}]_{\mathbf{s}, \mathbf{s}' \in \mathcal{S}}$ represent the $(M \times M)$ spatial correlation matrix such that the prior on each β_j is a zero-mean Gaussian random field with covariance $\zeta_j^2 \tau^2 \mathbf{C}$. Similarly, let Σ represent the variance of $\epsilon_i^w(\cdot)$, here an $(M \times M)$ diagonal matrix with the $\sigma^2(\mathbf{s})$, $\mathbf{s} \in \mathcal{S}$ on the diagonal; let \mathbf{X} denote the $(N \times P)$ matrix of participant-level covariates; let $\mathbf{y}_i = [y_i(\mathbf{s})]_{\mathbf{s} \in \mathcal{S}}$ denote the vectorized outcome image for participant i ; and let $\mathbf{y} = (\mathbf{y}_1^\top, \dots, \mathbf{y}_N^\top)^\top$ represent the $(NM \times 1)$ vector of concatenated subject outcomes.

With the data in this “long” format, the model can be conveniently expressed in terms of Kronecker products. With $\mathbf{Z} = \text{diag}(\zeta_0^2, \dots, \zeta_{P-1}^2)$, the conditional posterior variance of β can be written,

$$\text{var}(\beta \mid \mathbf{y}, \cdot) = (\mathbf{X}^\top \mathbf{X} \otimes \Sigma^{-1} + \mathbf{Z}^{-1} \otimes \tau^{-2} \mathbf{C}^{-1})^{-1}, \quad (10)$$

using shorthand to express conditioning on Σ , \mathbf{Z} , θ , and τ^2 . Since the dimension of β grows rapidly with P , it can be difficult or even impossible to work with (10) directly. Instead, we outline two strategies to enable efficient posterior computation at this scale. The first strategy, as alluded to above, is to replace \mathbf{C}^{-1} with a sparse approximation $\tilde{\mathbf{C}}^{-1}$ such that $\tilde{\mathbf{C}} \approx \mathbf{C}$. In doing so, we follow work on the so called “Nearest Neighbor Gaussian Process” (Datta et al., 2016; Finley et al., 2019), replacing the idea of k -nearest neighbors with small neighborhoods of fixed physical radius r . Briefly, we replace \mathbf{C}^{-1} with a conditional independence approximation, enforcing that $\tilde{\mathbf{C}}_{ij}^{-1} = 0$ if $d(\mathbf{s}_i, \mathbf{s}_j) > r$ for $\mathbf{s}_i, \mathbf{s}_j \in \mathcal{S}$. Similar ideas have been alternately called Vecchia approximation (Vecchia, 1988; Katzfuss and Guinness, 2021), composite likelihood (Varin et al., 2011), or Markov random field approximation (Rue and Held, 2005), but in general can lead to highly accurate and scalable approximations of full rank spatial models (see e.g., Taylor and Diggle, 2014; Datta et al., 2016; Heaton et al., 2019). Working with such an approximation of course introduces a hyperparameter, r , for the neighborhood radius size. In practice we found that in a large data setting choice of r had very little effect on our analysis (see Web Appendix D for a sensitivity analysis). In a small N setting, however, when the prior has more influence on the posterior, r must generally be chosen large enough to obtain a good approximation of the log prior. Anecdotally, we found that taking $r \geq 6$ mm worked well in simulation.

Although replacing \mathbf{C}^{-1} with $\tilde{\mathbf{C}}^{-1}$ in (10) above lends sparsity and efficiency to computation in our setting, it can still be burdensome to evaluate or decompose (10) even for moderate P . To overcome this issue we propose an approximate quasi-Newton Hamiltonian Monte Carlo (HMC) algorithm for sampling from the posterior of $\boldsymbol{\beta}$, conditional on the other model parameters. HMC is a hybrid, gradient-based MCMC method that is often more efficient in high dimensions than other MCMC algorithms (Neal, 2011), and can be used to avoid direct computation with the very high dimensional covariance matrix (10) here. In the general HMC algorithm, sampling can be improved by scaling the gradients by a carefully chosen “mass matrix,” \mathbf{M} . In their highly influential paper, Girolami and Calderhead showed that the most efficient choice updates \mathbf{M} to be proportional to the posterior Fisher information matrix of the updated parameter (Girolami and Calderhead, 2011). Instead, we can choose to use the prior information matrix to “estimate” the posterior information in the spirit of a quasi-Newton algorithm: doing so results in a computationally tractable and efficient alternative. Taking $\mathbf{M} \propto (\mathbf{Z}^{-1} \otimes \tau^{-2}\mathbf{C}^{-1})$ and plugging in a sparse approximation of \mathbf{C}^{-1} as above can result in dramatic improvement in Markov chain mixing with minimal increase in computation time. In practice, we found that we need not use the same $\tilde{\mathbf{C}}^{-1}$ in \mathbf{M} as in our approximation of the log prior. In fact, we found it better to use smaller neighborhood radii in our construction of \mathbf{M} , and that keeping the neighborhood radius within the 2–4 mm range here resulted in the best Markov chain mixing.

A.1 Computation for our working model

In this section we begin with a description of our posterior computation strategy for the working model, and then proceed by showing how this general plan can be modified to estimate the coefficients of our conditional and marginal model variants. Let $\boldsymbol{\Sigma}$ represent the variance of $\epsilon_i^w(\cdot)$, here an $(M \times M)$ diagonal matrix with the $\sigma^2(\mathbf{s})$, $\mathbf{s} \in \mathcal{S}$ on the diagonal; let \mathbf{X} denote the $(N \times P)$ matrix of participant-level covariates; let $\mathbf{y}_i = [y_i(\mathbf{s})]_{\mathbf{s} \in \mathcal{S}}$ denote the vectorized outcome image for participant i ; and let $\mathbf{y} = (\mathbf{y}_1^\top, \dots, \mathbf{y}_N^\top)^\top$. Finally, let $\mathbf{Z} = \text{diag}(\zeta_0^2, \dots, \zeta_{P-1}^2)$.

To help stabilize our computational steps, we first compute a rank revealing decomposition of the covariate matrix \mathbf{X} . We will work here with the singular value decomposition (SVD) $\mathbf{X} = \mathbf{U}\mathbf{D}\mathbf{V}^\top$, though the QR decomposition and its rank revealing variants, etc. would work in the same way. In general, computing the SVD is an $\mathcal{O}(NP^2)$ operation when $P \leq N$; even for relatively large P computing the SVD of \mathbf{X} takes minimal time compared to MCMC. For simplicity, we will assume here that \mathbf{X} is full column rank. Let $\boldsymbol{\gamma} = (\mathbf{V}^\top \otimes \mathbf{I}_M)\boldsymbol{\beta}$ denote our parameter of interest, rotated by \mathbf{V} . The effective prior on $\boldsymbol{\gamma}$

is simply,

$$\boldsymbol{\gamma} \sim \mathcal{N}(\mathbf{0}, \mathbf{V}^\top \mathbf{Z} \mathbf{V} \otimes \tau^2 \mathbf{C}),$$

which, as noted in the main text, can be efficiently approximated by plugging in a sparse matrix $\tilde{\mathbf{C}}^{-1}$ such that $\tilde{\mathbf{C}} \approx \mathbf{C}$. Given $C(\cdot)$ we can easily construct such a $\tilde{\mathbf{C}}^{-1}$ following recipes from (Finley et al., 2019). In turn, the log prior and its gradient can be approximated via,

$$\ln \pi(\boldsymbol{\gamma} \mid \mathbf{Z}, \boldsymbol{\theta}, \tau^2) \approx -\frac{1}{2} \boldsymbol{\gamma}^\top (\mathbf{V}^\top \mathbf{Z}^{-1} \mathbf{V} \otimes \tau^{-2} \tilde{\mathbf{C}}^{-1}) \boldsymbol{\gamma} + K(\mathbf{Z}, \boldsymbol{\theta}, \tau^2), \quad (11)$$

where $K(\mathbf{Z}, \boldsymbol{\theta}, \tau^2)$ is the log normalization constant and,

$$\nabla_{\boldsymbol{\gamma}} \ln \pi(\boldsymbol{\gamma} \mid \mathbf{Z}, \boldsymbol{\theta}, \tau^2) \approx -(\mathbf{V}^\top \mathbf{Z}^{-1} \mathbf{V} \otimes \tau^{-2} \tilde{\mathbf{C}}^{-1}) \boldsymbol{\gamma}. \quad (12)$$

Kronecker identities facilitate numerical evaluation of these quantities. Similarly, the log likelihood can be rewritten in terms of $\boldsymbol{\gamma}$. Up to the integration constant, the log likelihood of our working model can be written,

$$\ln \pi(\mathbf{y} \mid \boldsymbol{\Sigma}, \boldsymbol{\gamma}) = -\frac{1}{2} \boldsymbol{\gamma}^\top (\mathbf{D}^2 \otimes \boldsymbol{\Sigma}^{-1}) \boldsymbol{\gamma} + \boldsymbol{\gamma}^\top (\mathbf{D} \mathbf{U}^\top \otimes \boldsymbol{\Sigma}^{-1}) \mathbf{y} - \frac{1}{2} \mathbf{y}^\top (\mathbf{I}_N \otimes \boldsymbol{\Sigma}^{-1}) \mathbf{y}. \quad (13)$$

From this expression, it can be seen that the part of the log likelihood that includes $\boldsymbol{\gamma}$ depends on the data only through the sufficient statistic $(\mathbf{U}^\top \otimes \mathbf{I}_M) \mathbf{y}$. This implies that, within our working model framework, gradients and Metropolis-Hastings ratios can be computed efficiently with respect to $\boldsymbol{\gamma}$. Similarly, it can be shown that the residual sum of squares depends on the data only through $(\mathbf{U}^\top \otimes \mathbf{I}_M) \mathbf{y}$ and an additional sufficient statistic, $\sum_i \mathbf{y}_i^{\circ 2}$, where we use $\mathbf{a}^{\circ b} = (a_i^b)$ to denote element-wise or Hadamard exponentiation. This additional fact suggests that $\sigma^2(\cdot)$ can be easily updated without reference to the original data. With these two pieces in hand, we write our posterior computation algorithm to alternate updating $\boldsymbol{\gamma}$ through Hamiltonian Monte Carlo (as discussed in the main text), and updating the variance parameters with Gibbs sampling. Samples of $\boldsymbol{\gamma}$ can easily be rotated back into samples of $\boldsymbol{\beta}$ by applying the reverse transformation, $\boldsymbol{\beta} = (\mathbf{V} \otimes \mathbf{I}_M) \boldsymbol{\gamma}$. Within each HMC iteration, we update the algorithm's mass matrix via,

$$\mathbf{M}(\mathbf{Z}, \tau^2) = \mathbf{V}^\top \mathbf{Z}^{-1} \mathbf{V} \otimes \tau^{-2} \tilde{\mathbf{C}}_M^{-1}, \quad (14)$$

where $\tilde{\mathbf{C}}_M^{-1}$ is a sparse matrix again constructed so that $\tilde{\mathbf{C}}_M \approx \mathbf{C}$. We discussed the logic for doing this in the main text.

A.2 Approximation for our “Conditional” model

Our computational strategy for the conditional method relies on the observation that the full conditional distribution of the $\boldsymbol{\omega}_i$ is relatively easy to work with. Although it is too burdensome to fully sample the $\boldsymbol{\omega}_i$ at each iteration of an MCMC routine, it takes only a modest amount of time to find a maximum a posteriori (MAP) estimate of the $\boldsymbol{\omega}_i$ given an estimate of $\boldsymbol{\beta}$. As we have shown above, gradient-based updates are efficient to compute for $\boldsymbol{\beta}$ in our working model. We first obtain an approximate MAP estimate of $\boldsymbol{\beta}$ using our working model with the restriction that $\sigma^2(\mathbf{s}) \equiv \sigma^2$ for all locations $\mathbf{s} \in \mathcal{S}$. An estimate of this parameter can be computed quite quickly using gradient ascent. With estimates of $\boldsymbol{\beta}$, τ^2 , and $\boldsymbol{\Sigma}$ in hand, the $\boldsymbol{\omega}_i$ can be set to their conditional posterior mode analytically,

$$\boldsymbol{\omega}_i \leftarrow (\tau^{-2}\mathbf{C}^{-1} + \boldsymbol{\Sigma}^{-1})^{-1}\boldsymbol{\Sigma}^{-1}\{\mathbf{y}_i - (\mathbf{x}_i^\top \otimes \mathbf{I}_m)\boldsymbol{\beta}\}.$$

To do this, we again construct a sparse, Vecchia-type approximation of the matrix $(\tau^{-2}\mathbf{C}^{-1} + \boldsymbol{\Sigma}^{-1})^{-1}$. Maximizing with respect to $\boldsymbol{\beta}$ and $\boldsymbol{\omega}_i$ can be iterated if necessary for convergence. Once we have a satisfactory estimate of $\boldsymbol{\omega}_i$, we can easily subtract it from \mathbf{y}_i and switch to our working model HMC algorithm for inference on $\boldsymbol{\beta}$ if desired.

A.3 Approximation for our “Marginal” model

Rather than fix a point estimate of the $\boldsymbol{\omega}_i$ as above, our strategy for the marginal model will be instead to obtain a fixed estimate of the correlated error variance— $\mathbf{H} = \tau^2\mathbf{C} + \boldsymbol{\Sigma}$ in the main text—and use this estimate in our general HMC algorithm (described above). To compute with the marginal method, we first obtain an initial estimate of $\boldsymbol{\beta}$ using gradient ascent in our working model approximation as above. With this estimate in hand, we can estimate the marginal or sill variance $(\tau^2 + \sigma^2(\mathbf{s}))$ for each location \mathbf{s} using the standard formula $\sum_i \{y_i(\mathbf{s}) - \mathbf{x}_i^\top \boldsymbol{\beta}(\mathbf{s})\}^2 / (N - 1)$. Then, again following (Finley et al., 2019), it is straightforward to construct a Vecchia-type approximation $\tilde{\mathbf{H}}^{-1}$ such that $\tilde{\mathbf{H}} \approx \mathbf{H}$, and so that $\tilde{\mathbf{H}}$ contains our estimates of the spatial sills on the diagonal. To work with MCMC, $\tilde{\mathbf{H}}$ can simply be substituted in place of $\boldsymbol{\Sigma}$ in our working model HMC outline above. For computational savings, we do not update $\tilde{\mathbf{H}}$ over MCMC iterations when we work with the model in this way.

B Estimation of $\boldsymbol{\theta}$ through maximum marginal likelihood

In general spatial kriging applications, it is common to estimate $\boldsymbol{\theta}$ by maximum marginal likelihood (e.g., Mardia and Marshall, 1984; Rasmussen and Williams, 2006). This can

be done, for example by integrating out the mean model parameters and optimizing the resulting marginal likelihood with respect to the covariance and correlation parameters. Retaining the vector-based notation from our posterior computation sections and integrating the β_j and ω_i out of equation (1) in the main text, the marginal log likelihood (less the integration constant) for our spatial regression model is,

$$f(\mathbf{y} \mid \boldsymbol{\theta}, \boldsymbol{\Sigma}, \mathbf{Z}, \tau^2) = -\frac{1}{2} \sum_i \ln \det \boldsymbol{\Omega}_i + \mathbf{y}_i^\top \boldsymbol{\Omega}_i^{-1} \mathbf{y}_i, \quad (15)$$

where $\boldsymbol{\Omega}_i = \tau^2(1 + \sum_j \zeta_j^2 x_{ij}^2) \mathbf{C} + \boldsymbol{\Sigma}$, and $\boldsymbol{\Sigma}$ is the $(M \times M)$ sparse matrix with $[\sigma^2(\mathbf{s})]_{\mathbf{s} \in \mathcal{S}}$ on the diagonal. Equation (15) can of course be maximized directly, but at the cost of also solving for $M + P + 1$ additional parameters in $\boldsymbol{\Sigma}$, τ^2 , and the ζ_j^2 . Also, from a practical point of view, it is somewhat undesirable that the marginal variance of \mathbf{y}_i depends on \mathbf{x}_i , implying the need to re-optimize (15) every time a covariate is added to or removed from the model. Conceptually, it does not make much sense to imagine that the spatial correlation structure of the model mean parameters may change depending on the inclusion or exclusion of given covariates.

Instead of working with (15) directly, we choose to estimate $\boldsymbol{\theta}$ by optimizing the marginal log likelihood for a surrogate simpler model. To estimate $\boldsymbol{\theta}$, we replace (15) above with,

$$\tilde{f}(\mathbf{y} \mid \boldsymbol{\theta}, \boldsymbol{\Sigma}, \tau^2) = -\frac{N}{2} \ln \det(\tau^2 \mathbf{C} + \boldsymbol{\Sigma}) + -\frac{1}{2} \sum_i \mathbf{y}_i^\top (\tau^2 \mathbf{C} + \boldsymbol{\Sigma})^{-1} \mathbf{y}_i, \quad (16)$$

which, incidentally, is the unnormalized marginal likelihood for our working model with an intercept as the only predictor. Equation (16) can be evaluated approximately either through use of a Vecchia-type approximation of the matrix $(\tau^2 \mathbf{C} + \boldsymbol{\Sigma})^{-1}$, or by down-sampling the \mathbf{y}_i to a more manageable number of spatial locations. We chose the former option in the present paper, and in practice mean-center each image \mathbf{y}_i prior to optimization. While this approach can work well, we have noticed anecdotally that it can also tend to underestimate the width of the correlation function. Obtaining a good estimate of $\boldsymbol{\theta}$ in more complex settings—as in (15)—remains an open research question. We do not, however, expect inference on $\beta(\cdot)$ or other model parameters, to be overly sensitive to the choice of $\boldsymbol{\theta}$, given reasonable data (e.g. see our sensitivity analysis in Web Appendix D).

Finally, we have used the gradient-free optimization routine BOBYQA (Powell, 2009) to maximize (16), which, surprisingly, improved performance over gradient-based optimizers (both run time and stability). The BOBYQA algorithm works by iteratively constructing a quadratic approximation to the objective function at a set of interpolation points, which are themselves updated as a trust region is progressively estimated (Powell, 2009).

The algorithm may fail if, for example, (16) exhibits local behavior that cannot be well approximated by a quadratic function.

C Additional ABCD Study Data Description, Analysis, and Results

Data used in the preparation of this article were obtained from the Adolescent Brain Cognitive Development (ABCD) Study (<https://abcdstudy.org>), held in the NIMH Data Archive (NDA). This is a multisite, longitudinal study designed to recruit more than 10,000 children age 9-10 and follow them over 10 years into early adulthood. The ABCD Study is supported by the National Institutes of Health and additional federal partners under award numbers U01DA041048, U01DA050989, U01DA051016, U01DA041022, U01DA051018, U01DA051037, U01DA050987, U01DA041174, U01DA041106, U01DA041117, U01DA041028, U01DA041134, U01DA050988, U01DA051039, U01DA041156, U01DA041025, U01DA041120, U01DA051038, U01DA041148, U01DA041093, U01DA041089, U24DA041123, U24DA041147. A full list of supporters is available at <https://abcdstudy.org/federal-partners.html>. A listing of participating sites and a complete listing of the study investigators can be found at https://abcdstudy.org/consortium_members/. ABCD consortium investigators designed and implemented the study and/or provided data but did not necessarily participate in analysis or writing of this report. This manuscript reflects the views of the authors and may not reflect the opinions or views of the NIH or ABCD consortium investigators.

C.1 fMRI Preprocessing

Preprocessing of the fMRI task data was accomplished through use of a published standardized pipeline (see Sripada et al., 2021, “Supplemental FMRI Prep Methods”). Briefly, time series acquisitions were filtered with a 0.005 Hz high pass filter and spatially smoothed with a surface-based 2 mm kernel. Within patient task-based modeling was accomplished using tools from FSL (Jenkinson et al., 2012), removing high motion time points (frame-wise displacement > 0.9 mm) from the data. Additional regressors of no interest included 24 total motion parameters (linear and quadratic terms for each of six estimated motion parameters—three rotational, three translational—and their derivatives); five white matter principal components estimated with CompCor software (Behzadi et al., 2007); and five cerebrospinal fluid principal components also estimated with CompCor. Contrast images we analyzed in the present paper were derived from the results of these first-level task-based models.

C.2 Additional Data Description

Table 2: Demographic information for children in our sample. Continuous covariates are summarized by their mean, standard deviation and interquartile range; categorical covariates are summarized by percentage of the sample in the respective category.

Descriptor	Mean	SD	IQR
0-Back Accuracy	0.87	0.09	0.11
2-Back Accuracy	0.80	0.08	0.12
{0 - 2}-Back Difference	0.07	0.09	0.12
Age (yrs)	9.99	0.62	1.08
Fluid IQ	0.29	0.75	0.97
Percentage			
Child Gender			
Female	50.8%		
Male	49.2%		
Child Race/Ethnicity			
Asian	2.4%		
Black	8.8%		
Hispanic	17.1%		
Other	9.5%		
White	62.2%		
Household Income (US\$/yr)			
< 50K	22.4%		
50K–100K	30.7%		
≥ 100K	46.9%		
Parental Education			
< HS Diploma	2.1%		
HS Diploma/GED	5.3%		
Some College	23.0%		
Bachelor	28.6%		
Post Graduate Degree	41.0%		
Parental Marital Status			
Married Household	76.0%		
Unmarried Household	24.0%		

For this illustration we will work exclusively with data from a subset of 3,267 children in the baseline cohort that were scanned while performing an n-back task (Barch et al., 2013; Casey et al., 2018) with pictures of human faces expressing emotion as stimuli. The n-back task has enjoyed wide use in the neuropsychological and imaging community for its relationship with executive function and as a correlate of working memory processes (e.g., Jansma et al., 2000; Owen et al., 2005; Jaeggi et al., 2010). Our subsample of children

is limited to those who scored at or above 60% correct on both 0-back and 2-back task conditions.

Web Table 2 gives a summary of the demographic information for this sample. As a final note, the ABCD study more broadly contains imaging data acquired from siblings. Around 20% of families in the ABCD release 2.0 baseline data have two or more children enrolled in the study. This might additionally suggest the need for an analysis with random family effects. We avoid this issue entirely here: the cohort that we analyze contains data from only one child per family in our subset. While our method is capable of estimating effects like this in general, it would be very slow computationally to give a fully Bayesian treatment to a large number of random spatial effects. A more specific tool could be built on top of the methods we present here to include such variance components and/or treat them as nuisance parameters.

C.3 Additional Brain Region-Level Coefficient Summaries

Here we complete our report of demographic effects on the 2- vs 0-back task contrast data from the ABCD study. We again summarize results from the right hemisphere by averaging over all vertices within brain regions from the Gordon 2016 cortical surface parcellation (Gordon et al., 2016). Figures follow the same format as the primary model intercept and 2-back accuracy rate results figures from the main text. Results in the left hemisphere were generally highly symmetric.

As noted in the main text, covariates were chosen on the basis of known associations with n-back task accuracy (Pelegrina et al., 2015) and through preliminary exploratory analyses. Exploratory analyses served to help us visualize and understand several important aspects of the data. First, we observed modest but present nonlinear patterns in the relationship between the contrast data and 2-back accuracy. Preferring simplicity here, we found that these trends were reasonably well characterized by a quadratic model for 2-back accuracy. Including this term in the analysis resulted in a total of $P = 24$ predictors including the global intercept. We scaled each continuous covariate by two standard deviations (Gelman, 2008) so that resultant coefficient images are more directly comparable with coefficient images for categorical covariates.

Similarly to Fig. 4 in the main text, Web Fig. 7 summarizes results for the effect of 2-back accuracy rate on the 2- vs 0-back contrast. In the figure, coefficients for the linear and quadratic accuracy terms reflect the expected change in activation between ten year old female children scoring 96% and 80% correct on the 2-back condition, respectively, holding all other demographic covariates constant. Our analysis suggests high spatial overlap between the intercept and areas where average activation increased linearly with increasing

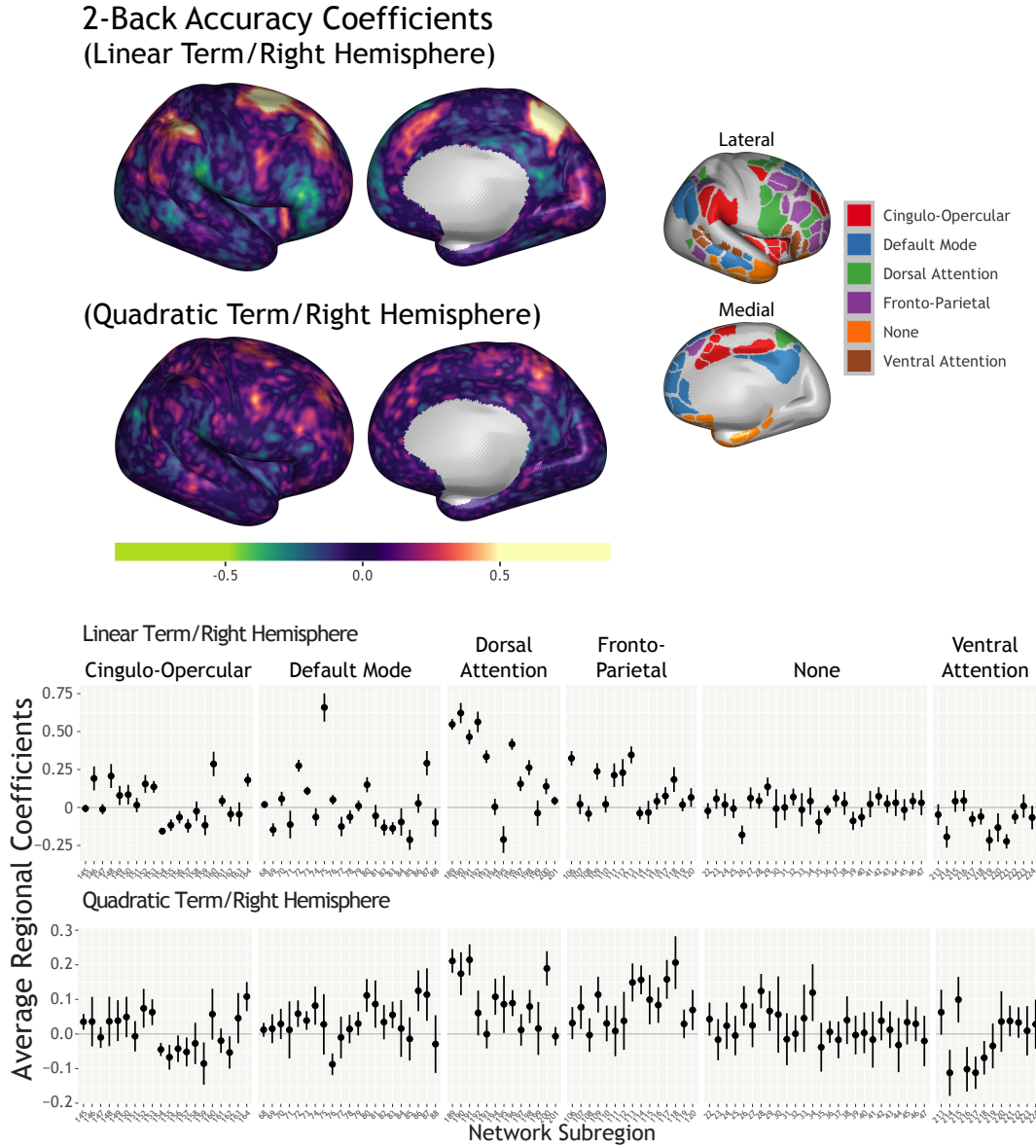


Figure 7: Coefficient summary for 2-back condition accuracy rate (linear and quadratic terms). The overall format of the figure is the same as in Fig. 4 in the main text.

2-back accuracy (confer from main text Fig. 4 and Web Fig. 7). Interestingly, however, the quadratic accuracy term largely seems to reflect areas where average activation increased supra-linearly with increasing 2-back accuracy. Based on our analysis, these areas are more constrained to regions associated with the Dorsal-Attention and Fronto-Parietal networks (Web Fig. 7).

Since the ABCD data are naturally grouped by the study's 21 data collection sites, we explored the utility of including random site effects. For these data, the random site effects

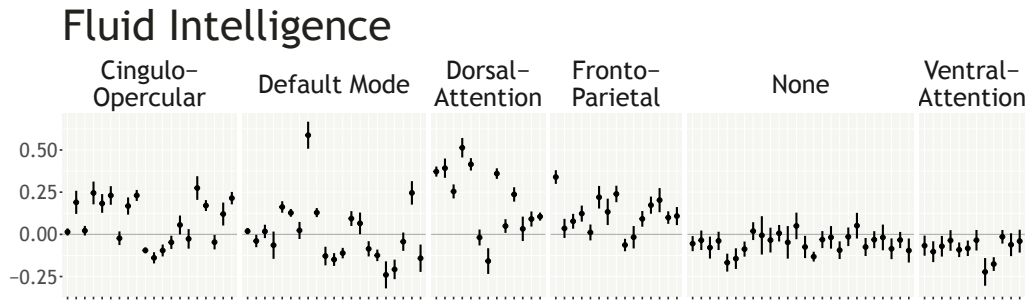


Figure 8: Regional average coefficients: fluid intelligence, linear term. Consistent with previous studies (e.g., Preusse et al., 2011; Li et al., 2021), fluid intelligence is positively correlated with task-related activation in functionally relevant cingulo-opercular, dorsal-attention, and fronto-parietal network regions.

explained less than 1% of the total variance in over 97% of vertices, and less than 0.1% of the variance in nearly half of vertices. We ultimately concluded that site-specific random effects do not critically influence results here. Again preferring simplicity, the results we show here and in the main text do not include site effects as a variance component. Web Fig. 14 displays posterior mean estimates of site effects for the five largest and five smallest collection sites.

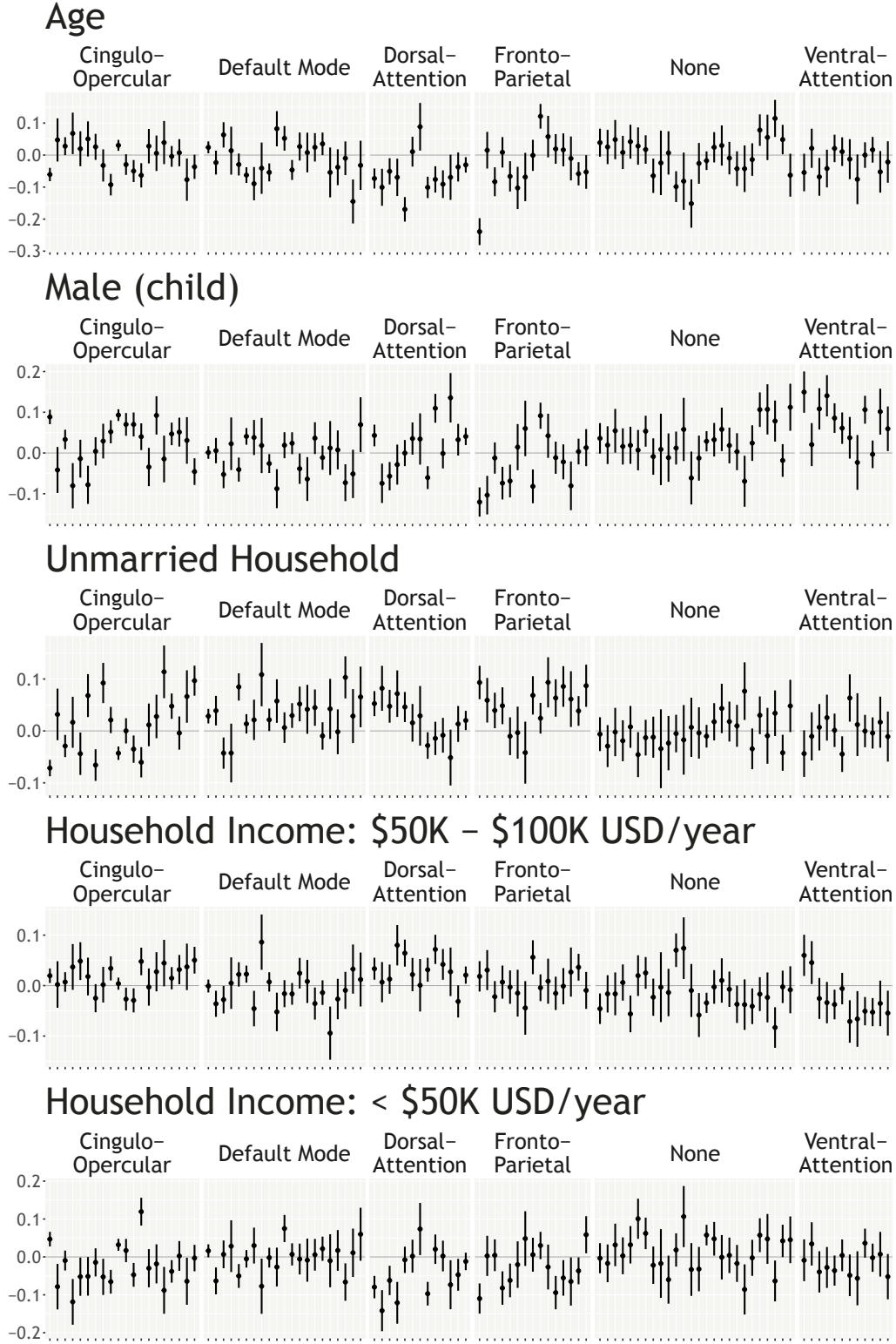


Figure 9: Regional average coefficients: additional demographic covariates. The majority of these effects are relatively small in magnitude with the notable exception of a negative association between child age and task-related activation in a functionally relevant fronto-parietal network region (Freesurfer label: 106).

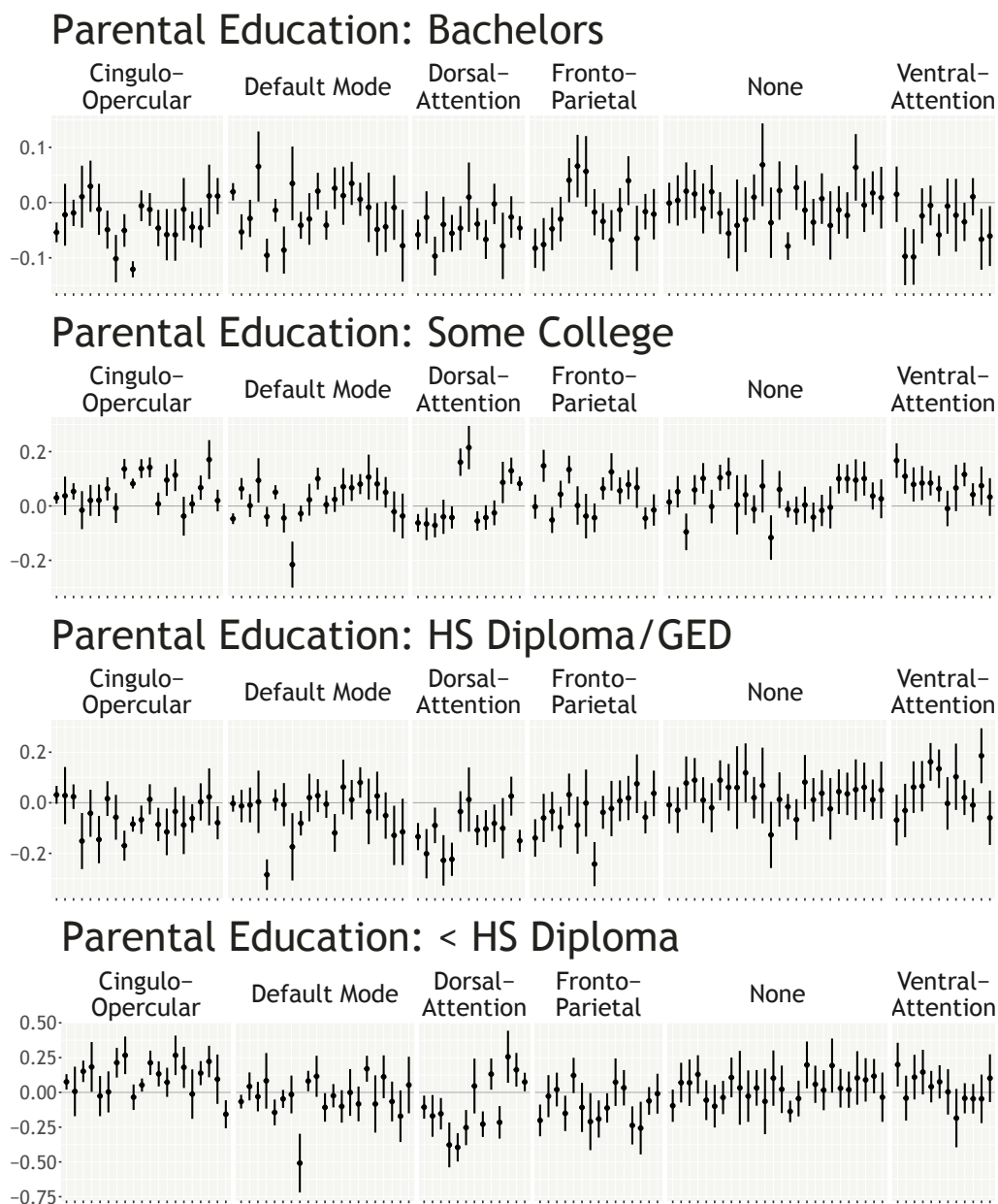


Figure 10: Regional average coefficients: parental education (compared to a “post-graduate degree” reference group). The largest magnitude effects may suggest a pattern of decreased activation in functionally relevant dorsal-attention and fronto-parietal network regions in children of parents with less than “some college” education.

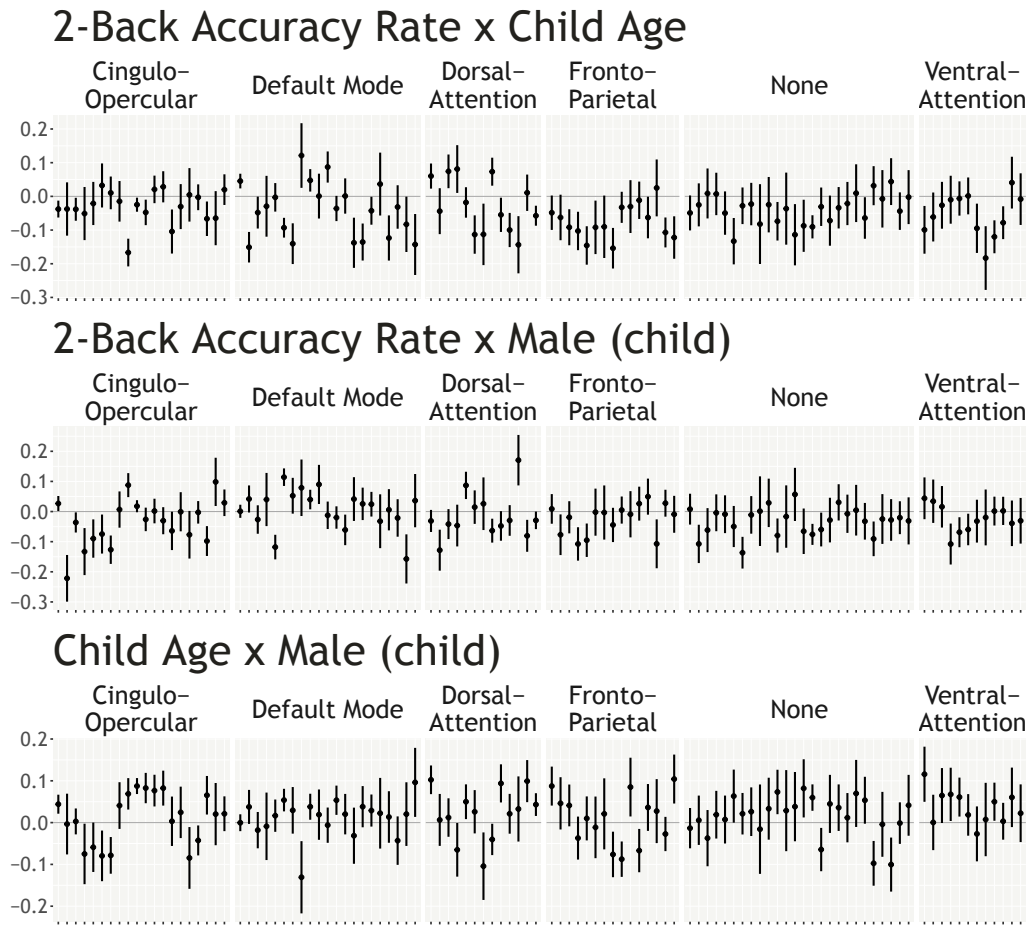


Figure 11: Regional average coefficients: first-order interaction terms between 2-back accuracy, child age, and child sex. Most effects here are relatively small in magnitude.

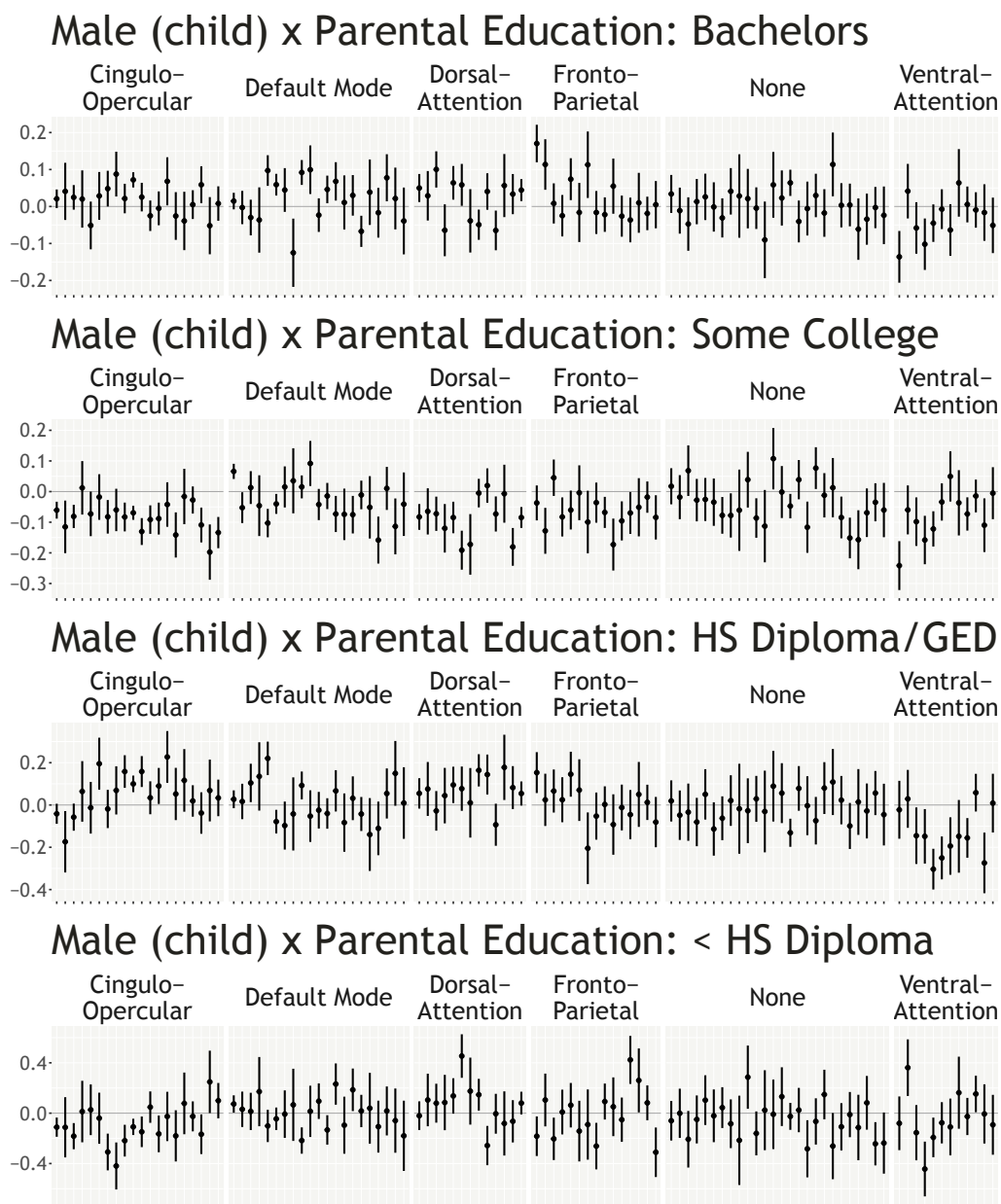


Figure 12: Regional average coefficients: first-order interaction terms between child sex and parental education. No clear pattern of results is apparent here as with the parental education main effect terms.

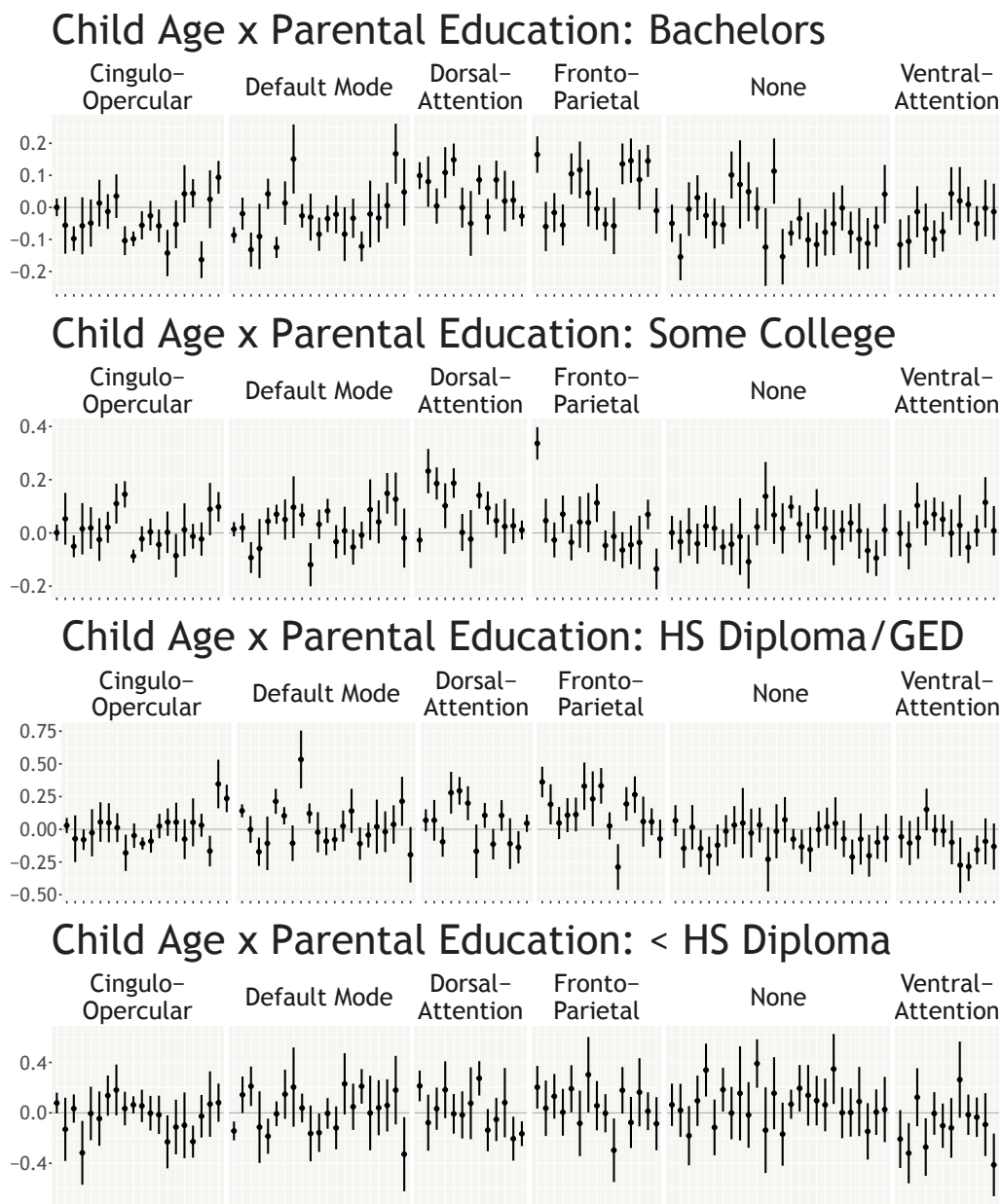


Figure 13: Regional average coefficients: first-order interaction terms between child age and parental education. The uncertainty in many of these coefficients is relatively large, but there appears to be a consistent pattern of positive interactions in functionally relevant dorsal-attention network regions. Interpretation of this result is somewhat complicated by the general pattern of negative coefficients for the main effects of child age and parental education in these same regions.

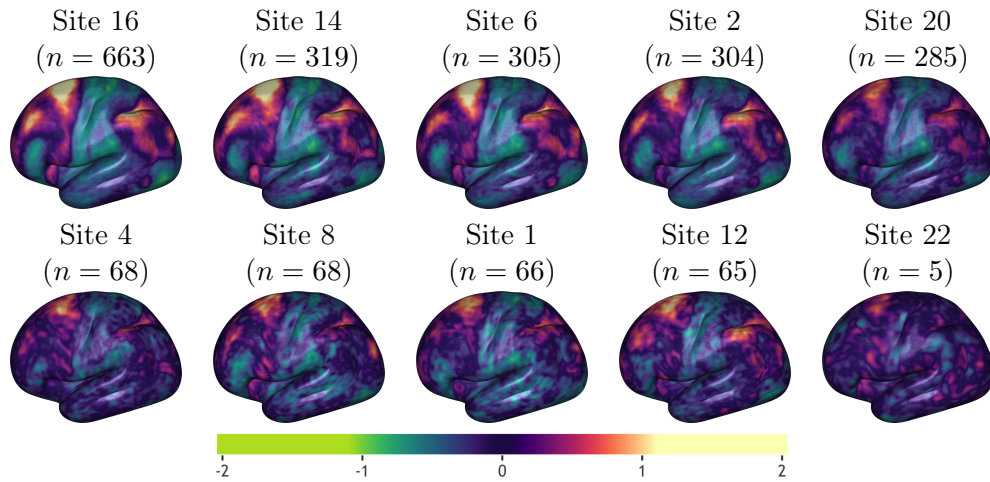


Figure 14: Site-specific effects for the five largest and five smallest sites in our ABCD study subset. We estimated the site-specific effects as random spatial intercepts using our working model framework. Site effects appear reasonably consistent across the 21 study locations, with of course smoother results evident for the largest sites.

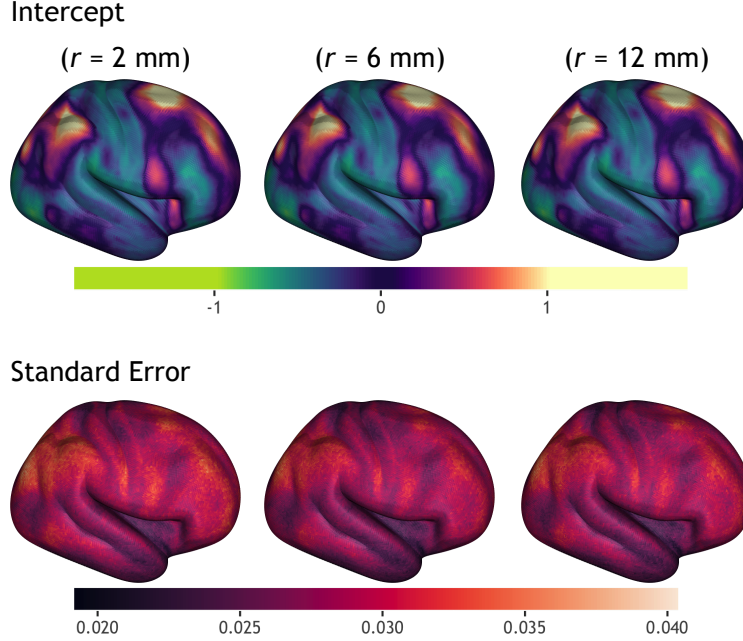


Figure 15: Sensitivity of model estimation to varying conditional independence neighborhood radii, r . Here, we explore the sensitivity of an intercept-only model for the ABCD study data at varying r .

D ABCD data analysis: MCMC diagnostics and sensitivity analyses

In this section we describe additional sensitivity analyses and MCMC diagnostics we have performed within the scope of the ABCD study data.

We fit our model with Hamiltonian Monte Carlo (HMC) as noted in the main text. For this analysis, we ran eight chains of 7,000 iterations each, discarding the first 5,000 as adaptation and burnin, and saving 200 samples from the final 2,000 iterations of each chain. Convergence was assessed via univariate folded and non-folded rank-normalized split \hat{R} (Vehtari et al., 2021) for each parameter $\beta_j(\cdot)$, and by visual examination of trace plots for subsets of these parameters. The folded split \hat{R} statistic was below the recommended threshold of 1.01 for over 99.9% of the $\beta_j(\cdot)$ (the worst case scenario was 1.02), indicating reasonable convergence in the posterior spread and tail behavior for these parameters. Similarly, the worst-case non-folded split \hat{R} statistic was 1.04 across all $\beta_j(\cdot)$, indicating reasonable convergence of the center of the posterior distribution for these parameters. We set the neighborhood radius of the Vecchia approximation of our prior precision to 8 mm, and the neighborhood radius of our HMC mass matrix to 3 mm. While the algorithm can be quite sensitive to the choice of mass matrix neighborhood radius, values in the range 2–4 mm

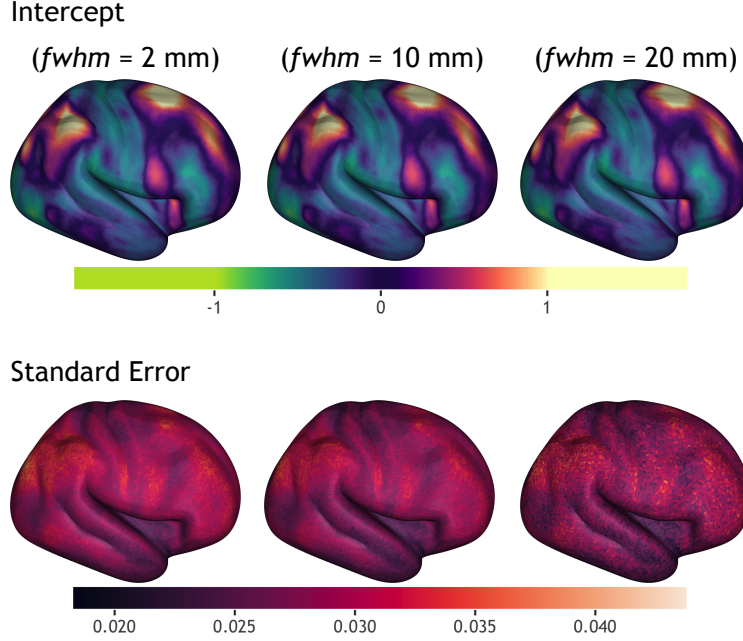


Figure 16: Sensitivity of model estimation to varying correlation function width. We again explored the sensitivity of an intercept-only model for the ABCD study data, this time for fixed r and correlation function family. Here, we have varied the width of the correlation function to explore the effect on estimation.

led to efficient and well-mixing chains both here and in simulation. For readers familiar with Hamiltonian Monte Carlo: Metropolis-Hastings rates were tuned during burnin to be approximately 65%; automatic tuning was achieved using the dual-averaging method presented in (Hoffman and Gelman, 2014). Additionally, we fixed the number of numerical integration steps in our HMC to 35, which we noted produced well-mixing chains.

We noted (in the main text and in Web Appendix A) that computationally we use a specific sparse precision matrix approximation to induce conditional independence between parameters at locations outside of an r -neighborhood of each other. A natural question in this context is how sensitive the analyses are to the choice of the neighborhood radius r . We briefly explored this question by repeatedly fitting our working model to the ABCD study data, using a spatial intercept as the only predictor, and varying r in the construction of our Vecchia approximation to the prior. Web Fig. 15 summarizes the results of this sensitivity analysis. In the figure, the posterior mean estimate (top row) is not visibly sensitive to the choice of r within a 2–12 mm range. The uncertainty in the spatial intercept (bottom row), moreover, is at worst only modestly sensitive to small r .

A related question is how sensitive results are to the correlation function parameters θ . As above, we repeatedly fit our working model using a spatial intercept as the only

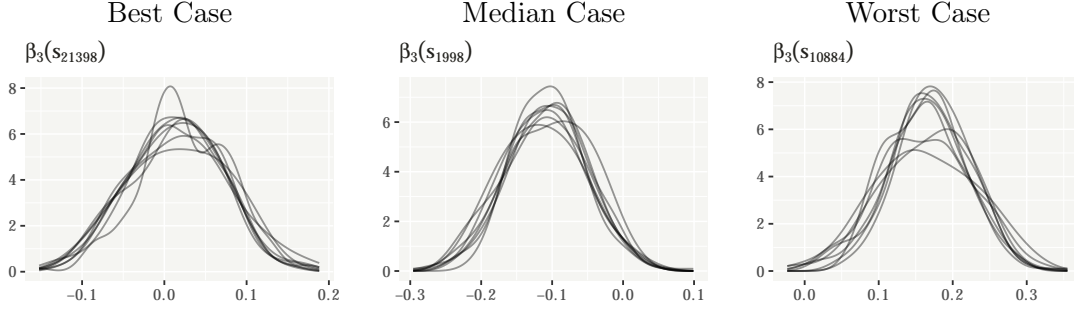


Figure 17: Density estimates of the posterior distribution of $\beta_3(\cdot)$ for three different vertices and constructed from 8 separate HMC chains. This diagnostic is for the analysis from the main text where $\beta_3(\cdot)$ represents the spatial coefficient function for the linear 2-back accuracy rate term. Selected vertices are rank-ordered from left to right by the corresponding split folded \hat{R} statistic for diagnosing MCMC convergence. The posterior densities appear to have converged reasonably well across the different chains.

predictor. For these analyses, we fixed our conditional independence neighborhood radius $r = 8$ mm and used radial basis correlation functions with exponent parameter 1.38 as in the main text. Here we varied only the width of the correlation to probe for sensitivity in the analysis. Web Fig. 16 summarizes the results of this analysis across the varying correlation widths. As before, the posterior mean (top row) is not visibly sensitive to the width of the correlation within a 2–20 mm range. The uncertainty in the spatial intercept (bottom row) is again modestly sensitive to the correlation width. The estimate of the spatial standard error for the 20 mm full-width-at-half-maximum correlation appears perhaps deteriorated (bottom right panel).

We also show an example MCMC convergence diagnostic for our analysis of ABCD study data from the main text. Web Fig. 17 shows representative posterior density estimates for the linear 2-back accuracy rate coefficient from three vertices, constructed from 8 HMC chains. In the figure, we have rank-ordered the selected vertices by the univariate split folded \hat{R} statistic (Vehtari et al., 2021) for MCMC convergence (left to right, $\hat{R} = 1$ to $\hat{R} = 1.01$). The posterior densities show reasonable convergence across the MCMC chains.

Finally, we give an informal comparison of realized estimation differences arising from use of our conditional, marginal, and working model variants in practice. For this comparison, we fit our various models to the real ABCD study data following the protocol described in the main text. Web Figs. 18 and 19 summarize the results of this comparison due to both modeling and algorithmic differences between the three methods. In particular, Web Fig. 18 shows how the posterior means of the $\beta_j(\mathbf{s})$ can be quite similar across our proposed methods despite differences in estimation strategy. Web Fig. 19 on the other

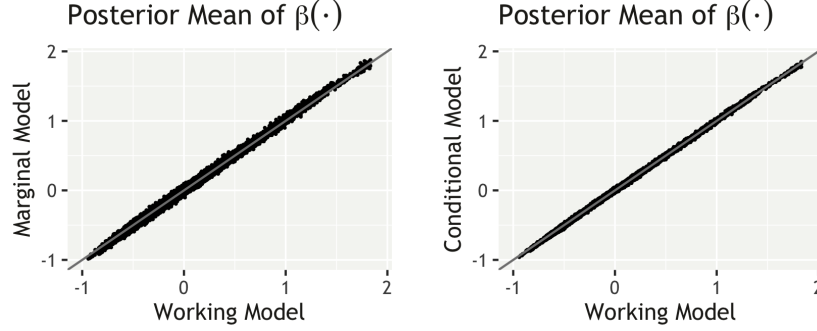


Figure 18: Comparison of the posterior mean of $\beta(\cdot)$ estimated from posterior samples drawn using each of our proposed conditional, marginal, and working model variants. Gray lines show identity relationships for reference.

hand shows that, relative to our working model variant, marginal posterior variances of the $\beta_j(\mathbf{s})$ were systematically larger for the marginal model and smaller for the conditional model in these data. We take these differences at face value here, and note only that in our simulation studies, both the marginal and working models performed quite well when data were generated directly from the conditional model (see e.g. Table 1 in the main text).

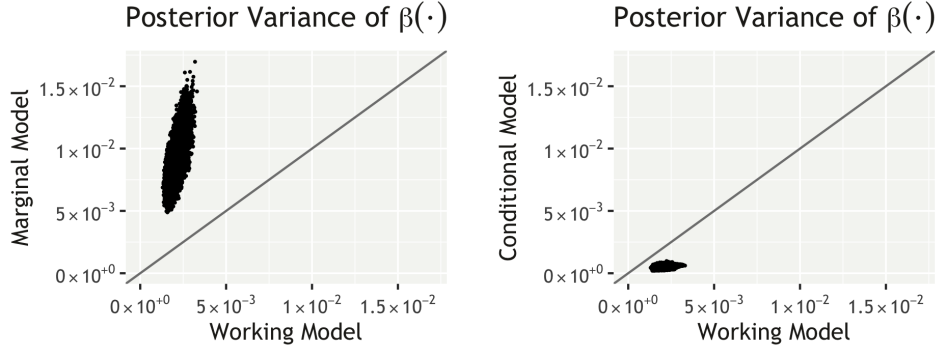


Figure 19: Comparison of the marginal posterior variances of each $\beta_j(\mathbf{s})$, $j \in 0, \dots, 23$ and $\mathbf{s} \in \mathcal{S}$, estimated from posterior samples drawn using each of our proposed conditional, marginal, and working model variants. Gray lines show identity relationships for reference.

References

Santiago Aja-Fernández, Tomasz Pie, Gonzalo Vegas-Sánchez-Ferrero, et al. Spatially variant noise estimation in MRI: A homomorphic approach. *Medical image analysis*, 20(1):

184–197, 2015.

Huda Akil, Maryann E Martone, and David C Van Essen. Challenges and opportunities in mining neuroscience data. *science*, 331(6018):708–712, 2011.

Margaret Armstrong. Improving the estimation and modelling of the variogram. In *Geostatistics for natural resources characterization*, pages 1–19. Springer, 1984.

Deanna M Barch, Gregory C Burgess, Michael P Harms, Steven E Petersen, Bradley L Schlaggar, Maurizio Corbetta, Matthew F Glasser, Sandra Curtiss, Sachin Dixit, Cindy Feldt, et al. Function in the human connectome: task-fMRI and individual differences in behavior. *Neuroimage*, 80:169–189, 2013.

Yashar Behzadi, Khaled Restom, Joy Liau, and Thomas T Liu. A component based noise correction method (compcor) for bold and perfusion based fmri. *Neuroimage*, 37(1):90–101, 2007.

Alexander Bowring, Fabian JE Telschow, Armin Schwartzman, and Thomas E Nichols. Confidence sets for cohen’s d effect size images. *NeuroImage*, 226:117477, 2021.

Stefan Brodoehl, Christian Gaser, Robert Dahnke, Otto W Witte, and Carsten M Klingner. Surface-based analysis increases the specificity of cortical activation patterns and connectivity results. *Scientific reports*, 10(1):1–13, 2020.

BJ Casey, Tariq Cannonier, May I Conley, Alexandra O Cohen, Deanna M Barch, Mary M Heitzeg, Mary E Soules, Theresa Teslovich, Danielle V Dellarco, Hugh Garavan, et al. The adolescent brain cognitive development (ABCD) study: imaging acquisition across 21 sites. *Developmental cognitive neuroscience*, 32:43–54, 2018.

David F. Cechetto and Jane C. Topolovec. Cerebral cortex. In Vilayanur S Ramachandran, editor, *Encyclopedia of the Human Brain Set/VS Ramachandran/2002 Academic Press-Elsevier Science USA.*, pages 663–679. 2002 Academic Press-Elsevier Science USA, New York, 2002. ISBN 978-0-12-227210-3. doi: <https://doi.org/10.1016/B0-12-227210-2/00087-X>. URL <https://www.sciencedirect.com/science/article/pii/B012227210200087X>.

Noel Cressie and Gary Glonek. Median based covariogram estimators reduce bias. *Statistics & probability letters*, 2(5):299–304, 1984.

Abhirup Datta, Sudipto Banerjee, Andrew O Finley, and Alan E Gelfand. Hierarchical nearest-neighbor Gaussian process models for large geostatistical datasets. *Journal of the American Statistical Association*, 111(514):800–812, 2016.

- SW Feldstein-Ewing and M Luciana. The Adolescent Brain Cognitive Development (ABCD) consortium: Rationale, aims, and assessment strategy. *Developmental Cognitive Neuroscience*, 32:1–164, 2018.
- Andrew O Finley, Abhirup Datta, Bruce D Cook, Douglas C Morton, Hans E Andersen, and Sudipto Banerjee. Efficient algorithms for Bayesian nearest neighbor Gaussian processes. *Journal of Computational and Graphical Statistics*, 28(2):401–414, 2019.
- Bruce Fischl, Martin I Sereno, and Anders M Dale. Cortical surface-based analysis: II: inflation, flattening, and a surface-based coordinate system. *Neuroimage*, 9(2):195–207, 1999a.
- Bruce Fischl, Martin I Sereno, Roger BH Tootell, and Anders M Dale. High-resolution intersubject averaging and a coordinate system for the cortical surface. *Human brain mapping*, 8(4):272–284, 1999b.
- H Garavan, H Bartsch, K Conway, A Decastro, RZ Goldstein, S Heeringa, T Jernigan, A Potter, W Thompson, and D Zahs. Recruiting the ABCD sample: Design considerations and procedures. *Developmental cognitive neuroscience*, 32:16–22, 2018.
- Alan E Gelfand, Hyon-Jung Kim, CF Sirmans, and Sudipto Banerjee. Spatial modeling with spatially varying coefficient processes. *Journal of the American Statistical Association*, 98(462):387–396, 2003.
- Andrew Gelman. Scaling regression inputs by dividing by two standard deviations. *Statistics in medicine*, 27(15):2865–2873, 2008.
- Andrew Gelman, Xiao-Li Meng, and Hal Stern. Posterior predictive assessment of model fitness via realized discrepancies. *Statistica sinica*, pages 733–760, 1996.
- Mark Girolami and Ben Calderhead. Riemann manifold Langevin and Hamiltonian Monte Carlo methods. *Journal of the Royal Statistical Society: Series B (Statistical Methodology)*, 73(2):123–214, 2011.
- Evan M Gordon, Timothy O Laumann, Babatunde Adeyemo, Jeremy F Huckins, William M Kelley, and Steven E Petersen. Generation and evaluation of a cortical area parcellation from resting-state correlations. *Cerebral cortex*, 26(1):288–303, 2016.
- Matthew J Heaton, Abhirup Datta, Andrew O Finley, Reinhard Furrer, Joseph Guinness, Rajarshi Guhaniyogi, Florian Gerber, Robert B Gramacy, Dorit Hammerling, Matthias Katzfuss, et al. A case study competition among methods for analyzing large spatial

- data. *Journal of Agricultural, Biological and Environmental Statistics*, 24(3):398–425, 2019.
- Matthew D Hoffman and Andrew Gelman. The No-U-Turn sampler: adaptively setting path lengths in Hamiltonian Monte Carlo. *Journal of Machine Learning Research*, 15(1):1593–1623, 2014.
- Susanne M Jaeggi, Martin Buschkuhl, Walter J Perrig, and Beat Meier. The concurrent validity of the n-back task as a working memory measure. *Memory*, 18(4):394–412, 2010.
- Johan Martijn Jansma, Nick F Ramsey, Richard Coppola, and René S Kahn. Specific versus nonspecific brain activity in a parametric n-back task. *Neuroimage*, 12(6):688–697, 2000.
- Mark Jenkinson, Christian F Beckmann, Timothy EJ Behrens, Mark W Woolrich, and Stephen M Smith. Fsl. *Neuroimage*, 62(2):782–790, 2012.
- Terry L Jernigan, Betty Casey, Duncan Clark, Ian Colrain, Anders Dale, Thomas Ernst, Raul Gonzalez, Mary Heitzeg, Krista Lisdahl, Monica Luciana, Bonnie Nagel, Elizabeth Sowell, Lindsay Squeglia, Susan Tapert, and Deborah Yurgeluntodd. Adolescent Brain Cognitive Development study (ABCD) 2.0.1 release #721, 2019. URL <https://nda.nih.gov/study.html?id=721>.
- Edward G Jones and Alan Peters. *Cerebral Cortex: Comparative Structure and Evolution of Cerebral Cortex, Part II*, volume 8. Springer Science & Business Media, 2012.
- Matthias Katzfuss and Joseph Guinness. A general framework for Vecchia approximations of Gaussian processes. *Statistical Science*, 36(1):124–141, 2021.
- Guangfei Li, Yu Chen, Thang M Le, Wuyi Wang, Xiaoying Tang, and Chiang-Shan R Li. Neural correlates of individual variation in two-back working memory and the relationship with fluid intelligence. *Scientific reports*, 11(1):1–13, 2021.
- M Luciana, JM Bjork, BJ Nagel, DM Barch, R Gonzalez, SJ Nixon, and MT Banich. Adolescent neurocognitive development and impacts of substance use: Overview of the adolescent brain cognitive development (ABCD) baseline neurocognition battery. *Developmental cognitive neuroscience*, 32:67–79, 2018.
- Kanti V Mardia and Roger J Marshall. Maximum likelihood estimation of models for residual covariance in spatial regression. *Biometrika*, 71(1):135–146, 1984.
- Amanda F Mejia, Yu Yue, David Bolin, Finn Lindgren, and Martin A Lindquist. A Bayesian general linear modeling approach to cortical surface fMRI data analysis. *Journal of the American Statistical Association*, 115(530):501–520, 2020.

- Michal Mikl, Radek Mareček, Petr Hlušík, Martina Pavlicová, Aleš Drastich, Pavel Chlebus, Milan Brázdil, and Petr Krupa. Effects of spatial smoothing on fMRI group inferences. *Magnetic resonance imaging*, 26(4):490–503, 2008.
- Jeanette A Mumford and Thomas Nichols. Simple group fMRI modeling and inference. *Neuroimage*, 47(4):1469–1475, 2009.
- Radford M Neal. MCMC using Hamiltonian dynamics. *Handbook of markov chain monte carlo*, 2(11):2, 2011.
- Thomas E Nichols and Andrew P Holmes. Nonparametric permutation tests for functional neuroimaging: a primer with examples. *Human brain mapping*, 15(1):1–25, 2002.
- Adrian M Owen, Kathryn M McMillan, Angela R Laird, and Ed Bullmore. N-back working memory paradigm: A meta-analysis of normative functional neuroimaging studies. *Human brain mapping*, 25(1):46–59, 2005.
- Santiago Pelegrina, M Teresa Lechuga, Juan A García-Madruga, M Rosa Elosúa, Pedro Macizo, Manuel Carreiras, Luis J Fuentes, and M Teresa Bajo. Normative data on the n-back task for children and young adolescents. *Frontiers in psychology*, 6:1544, 2015.
- William D Penny, Nelson J Trujillo-Barreto, and Karl J Friston. Bayesian fMRI time series analysis with spatial priors. *NeuroImage*, 24(2):350–362, 2005.
- Michael JD Powell. The BOBYQA algorithm for bound constrained optimization without derivatives. *Cambridge NA Report NA2009/06*, University of Cambridge, Cambridge, 26, 2009.
- Franziska Preusse, Elke Van Der Meer, Gopikrishna Deshpande, Frank Krueger, and Isabell Wartenburger. Fluid intelligence allows flexible recruitment of the parieto-frontal network in analogical reasoning. *Frontiers in human neuroscience*, 5:22, 2011.
- Carl Edward Rasmussen and Joaquin Quinonero-Candela. Healing the relevance vector machine through augmentation. In *Proceedings of the 22nd international conference on Machine learning*, pages 689–696, 2005.
- Carl Edward Rasmussen and Christopher KI Williams. *Gaussian processes for machine learning*, chapter Model Selection and Adaptation of Hyperparameters, pages 105–128. Number 5. MIT press Cambridge, MA, 2006.
- Martin Reuter, H Diana Rosas, and Bruce Fischl. Highly accurate inverse consistent registration: a robust approach. *NeuroImage*, 53(4):1181–1196, 2010.

- Donald B Rubin. Bayesianly justifiable and relevant frequency calculations for the applied statistician. *The Annals of Statistics*, pages 1151–1172, 1984.
- Havard Rue and Leonhard Held. *Gaussian Markov random fields: Theory and applications*. Chapman and Hall/CRC, 2005.
- Håvard Rue, Andrea Riebler, Sigrunn H Sørbye, Janine B Illian, Daniel P Simpson, and Finn K Lindgren. Bayesian computing with INLA: a review. *Annual Review of Statistics and Its Application*, 4:395–421, 2017.
- David Ruppert, Matt P Wand, and Raymond J Carroll. *Semiparametric regression*, chapter Inference, pages 133–160. Number 12. Cambridge university press, 2003.
- Per Sidén, Anders Eklund, David Bolin, and Mattias Villani. Fast Bayesian whole-brain fMRI analysis with spatial 3D priors. *NeuroImage*, 146:211–225, 2017.
- Michael A Silver and Sabine Kastner. Topographic maps in human frontal and parietal cortex. *Trends in cognitive sciences*, 13(11):488–495, 2009.
- Stephen M Smith and Thomas E Nichols. Statistical challenges in “big data” human neuroimaging. *Neuron*, 97(2):263–268, 2018.
- Chandra Sripada, Mike Angstadt, Aman Taxali, D Angus Clark, Tristan Greathouse, Saige Rutherford, Joseph R Dickens, Kerby Shedden, Arianna M Gard, Luke W Hyde, et al. Brain-wide functional connectivity patterns support general cognitive ability and mediate effects of socioeconomic status in youth. *Translational psychiatry*, 11(1):1–8, 2021.
- Michael L Stein et al. Spatial variation of total column ozone on a global scale. *The Annals of Applied Statistics*, 1(1):191–210, 2007.
- Shu-Chih Su, Brian Caffo, Elizabeth Garrett-Mayer, and Susan Spear Bassett. Modified test statistics by inter-voxel variance shrinkage with an application to fMRI. *Biostatistics*, 10(2):219–227, 2009.
- Benjamin M Taylor and Peter J Diggle. INLA or MCMC? A tutorial and comparative evaluation for spatial prediction in log-Gaussian Cox processes. *Journal of Statistical Computation and Simulation*, 84(10):2266–2284, 2014.
- Bertrand Thirion. *Handbook of Neuroimaging Data Analysis*, chapter Functional neuroimaging group studies, pages 335–354. Number 12. Chapman & Hall/CRC, 2016.
- John Darrell Van Horn and Arthur W Toga. Multi-site neuroimaging trials. *Current opinion in neurology*, 22(4):370, 2009.

- Cristiano Varin, Nancy Reid, and David Firth. An overview of composite likelihood methods. *Statistica Sinica*, pages 5–42, 2011.
- Aldo V Vecchia. Estimation and model identification for continuous spatial processes. *Journal of the Royal Statistical Society: Series B (Methodological)*, 50(2):297–312, 1988.
- Aki Vehtari, Andrew Gelman, Daniel Simpson, Bob Carpenter, and Paul-Christian Bürkner. Rank-normalization, folding, and localization: An improved \hat{R} for assessing convergence of MCMC (with discussion). *Bayesian analysis*, 16(2):667–718, 2021.
- Nora D Volkow, George F Koob, Robert T Croyle, Diana W Bianchi, Joshua A Gordon, Walter J Koroshetz, Eliseo J Pérez-Stable, William T Riley, Michele H Bloch, Kevin Conway, et al. The conception of the ABCD study: From substance use to a broad NIH collaboration. *Developmental cognitive neuroscience*, 32:4–7, 2018.
- Bo Wang and D Michael Titterington. Inadequacy of interval estimates corresponding to variational Bayesian approximations. In *International Workshop on Artificial Intelligence and Statistics*, pages 373–380. PMLR, 2005.
- Guoqing Wang, John Muschelli, and Martin A Lindquist. Moderated t-tests for group-level fMRI analysis. *NeuroImage*, 237:118141, 2021.
- Mark William Woolrich, Mark Jenkinson, J Michael Brady, and Stephen M Smith. Fully Bayesian spatio-temporal modeling of fMRI data. *IEEE transactions on medical imaging*, 23(2):213–231, 2004.